Disease-relevant single cell photonic signatures identify S100β^{+} stem cells and their myogenic progeny in vascular lesions

Claire Molony[¶1], Damien King[¶2], Mariana Di Luca[1], Abidemi Olayinka[1], Roya Hakimjavadi[1], Lourdes A.N. Julius[2], Emma Fitzpatrick[1], Denise Burtenshaw[1], Killian Healy[2], Emma Finlay[3], David Kernan[2], Andreu Llobera[4], Weimin Liu[5], David Morrow[5], Eileen M. Redmond[5], Jens Ducrée[2] Paul A. Cahill[1]*

[1] Vascular Biology and Therapeutics Laboratory, School of Biotechnology Faculty of Science and Health, Dublin City University, Dublin 9, Ireland.
[2] Fraunhofer Project Centre for Embedded BioAnalytical Systems, Faculty of Science and Health, Dublin City University, Dublin 9, Ireland.
[3] School of Biotechnology Faculty of Science and Health, Dublin City University, Dublin 9, Ireland
[4] Centre Nacional de Microelectronica, Campus UAB, Barcelona, Spain.
[5]Department of Surgery, University of Rochester Medical Center, Rochester, NY USA.

*To whom correspondence should be addressed:
Tel: (353) 1-700-8466
Fax: (353) 1-700-5412
e-mail: paul.cahill@dcu.ie

Summary

Vascular lesions enriched with smooth muscle (SMC)-like cells contribute to the development of subclinical atherosclerosis yet the origin of these cells remains controversial. Herein, we combine single cell label-free photonics with lineage tracing analysis to examine the cellular heterogeneity of vascular cells within lesions. Single cell autofluorescence emissions from normal and injured vessels *ex vivo* were compared to aortic SMCs, cultured Movas SMCs, macrophages, B-cells, S100β$^+$ resident vascular stem cells (mVSc), mesenchymal stem cells (MSC) and their myogenic progeny across five wavelengths λ465 - λ670 ± 20 nm. Principal component analysis (PCA) revealed discrete photonic signatures, particularly at λ565 nm, that reflect cell type and differentiation state. Supervised machine learning using multilayer perceptron (MLP) neural network analysis, linear discriminant analysis (LDA), and lineage tracing of S100β$^+$ mVSc identified the presence of mVSc and their myogenic progeny within injured vessels. We conclude disease-relevant photonic signatures may have predictive value for vascular disease.

Keywords: arteriosclerosis, intimal formation, resident vascular stem cells, smooth muscle cells, photonics, neural network analysis, hedgehog, Notch, TGF-β1.

Introduction

Cardiovascular disease (CVD), the leading cause of death and disability world-wide is characterized by pathological structural changes to the blood vessel wall [1]. A hallmark is the accumulation of smooth muscle cell (SMC)-like cells leading to intimal medial thickening (IMT) and the obstruction to blood flow that may culminate in a heart attack or stroke [2]. Pathologic observations in humans vessels confirm that early 'transitional' lesions enriched with SMC-like cells are routinely present in atherosclerotic-prone regions of arteries during pathologic intimal thickening, lipid retention, and the appearance of a developed plaque [3]. Endothelial cell (EC) dysfunction due to disturbed blood flow is classically associated with the development of atheroprone lesions [4–6]. These early lesions represent an important therapeutic target and are routinely modelled in mouse carotid arteries following flow restriction caused by ligation [7]. These ligation-induced lesions can further develop into advanced atherosclerotic plaques in *ApoE* knockout mice on Western diets [8,9].

Lineage tracing analysis has provided compelling evidence for the involvement of a population of (i) differentiated myosin heavy chain 11 (Myh11)$^+$ medial SMC in progressing intimal thickening in various animal models [10–14] and (ii) adventitial and medial progenitors in progressing intimal thickening [15–20]. While some adventitial progenitors are derived from a parent Myh11$^+$ SMC population [17], non-SMC derived SRY-related HMG-box 10 (Sox10) adventitial/medial resident multipotent vascular stem cells (MVSC) and Nestin$^+$ progenitor cells have also been implicated [19,20]. Single cell RNA sequence analysis (scRNA-seq) further suggested that a rare subpopulation of Myh11-Cre marked SMC that are stem cell antigen-1 positive (Sca1$^+$) may be entirely responsible [21] while cell fate mapping and scRNA-seq studies also implicated non-SMC adventitial Sca1$^+$ cells as they expand more rapidly than pre-existing SMCs within severe lesions [22]. Despite these insights, the putative role of resident vascular stem cells that do not originate from medial Myh11$^+$ SMCs in promoting intimal thickening remains controversial.

Several key modulators of vascular SMC phenotype and fate have been reported. Transforming growth factor (TGF-β1) is a key cytokine regulating myogenic differentiation [23]. TGF-β1 is released by both inflammatory cells and vascular cells [endothelial (EC) and SMC] [24,25] within the vessel wall. Importantly, elevated TGF-β1 levels and altered downstream

signalling have been implicated in the etiology of atherosclerosis [26], vessel restenosis [27] and in the development of the neointima [28]. Genome-wide association studies have also identified chromosome 14q32 as a locus for a hitherto uncharacterized gene called HHIPL1 (Hedgehog interacting protein-like 1)[29] which encodes a sequence homolog of an antagonist of hedgehog signalling that is secreted as a pro-atherogenic protein to regulate lesion formation [30]. Furthermore, Notch signalling may direct lesion formation by modulating the function of EC, SMCs, macrophages and stem cells [31–36].

In a post-genomic era, information-rich technologies are proving critically important drivers for both fundamental biology and personalised medicine [37]. In particular, scRNA-seq clustering has elucidated cell-to-cell heterogeneity and uncovered cell subgroups and cell dynamics in numerous systems [38], including vascular [21,22,39]. Label-free technologies for bio-analytical applications have also attracted recent attention with several different classes of label-free sensor detectors now being developed, including plasmonic, photonic, electrical and mechanical sensors [40]. Light as a diagnostic and prognostic tool has several potential advantages including high sensitivity, non-destructive measurement, small or even non-invasive analysis and low limits of detection [41]. The innate optical response comprises of scattering, absorbance, and auto-fluorescence signals. Importantly, the combination of several fluorescence and/or absorbance bands together with scattering bands form a specific spectral response which is unique for each particular cell (photonic signature). The amount, distribution, specific photonic properties and microenvironment of endogenous fluorophores present within individual cells and tissues collectively influence the overall emission signal. These autofluorescence emissions are closely associated with metabolism or structure of organs under normal, altered or pathological conditions [42–44]. In combination with microfluidics, photonics enables real time measurement of relevant analytes in very small sample volumes [45]. In this context, we have developed label-free photonic technologies with highly efficient cell-to-light coupling that have been successfully deployed to measure the real-time response of individual cells in a population [46,47]. Deep learning, a subset of machine learning based primarily on artificial neural network geometries, has rapidly grown in the bio-photonic field as a predictive method to obtain real-time bio-photonic decision-making systems and analyse bio-photonic data, in particular, spectroscopic data including spectral data pre-processing and spectral classification [48,49].

In the present study, we combine single cell label-free optical multi-parameter interrogation of cells *ex vivo* with lineage tracing analysis of resident S100β^{+} murine vascular stem cells (mVSc) *in vivo* to examine the cellular heterogeneity of vascular lesions following iatrogenic flow restriction. We determined whether the photonic profile due to autofluorescence emissions of single cells within injured vessels shared spectral similarity with aortic SMCs, macrophages, B-cells, bone-marrow-derived mesenchymal stem cells and resident S100β mVSc before and after myogenic differentiation *in vitro,* and moreover, whether the native fluorophores, elastin and collagen III (Coll 3A1) contributed in part to these similarities. Lineage tracing analysis of S100β^{+} mVSc and their progeny in conjunction with linear discriminant analysis (LDA) and supervised machine learning using a multilayer perceptron (MLP) artificial neural network of these trained spectral datasets was then deployed to classify all cells and interrogate injured vessels for the presence of these cells.

Results

Single cell photonics from normal and injured vessels *ex vivo* following flow restriction

The left carotid artery (LCA) of mice was isolated, sectioned and H&E stained following sham-operation or partial-ligation for 14 d [Figure 1A]. Morphometric analysis of the LCA confirmed a significant increase in adventitial and intimal volumes when compared to sham control [Figure 1B]. Immunohistochemical analysis of Myh11 expression in the medial (M) layers of sham, and the medial (M) and neointimal (NI) layers of ligated LCA vessels revealed a significant reduction in the number of Myh11^{+} positive cells in LCA after ligation [Figure 1C]. Medial sham SMC and medial and neointimal SMC-like cells within ligated vessels robustly expressed smooth muscle cell α-actin (SMA) [Figure 1C]. Myh11 protein expression in lysates from ligated LCA was also markedly reduced when compared to the sham control [Figure 1D].

To delineate cell heterogeneity in normal and injured vessels, we initially generated photonic profiles of individual cells using single cell autofluorescence emissions across five broadband light wavelengths (λ465, λ530, λ565, λ630 and λ670 with a bandwidth of 20 nm) captured on V-cups using a centrifugal Lab-on-a-Disc (LoaD) platform, as previously described [47] [Figure 1E]. Single cells were isolated from the medial layer of mouse carotid arteries by enzymatic digestion following removal of the adventitia and endothelium. The formalin-fixed cells were visualised by phase contrast microscopy on each V-cup [Figure 1F]. The Log10 autofluorescence emissions of 356 cells from 6 animals/group were recorded across all five wavelengths [Figure 1G] and corrected as Log2 fold increase over background [Figure 1H]. The photonic intensity of single cells from the ligated vessels *ex vivo* was significantly enhanced at the first 3 wavelengths (λ465, λ530 and λ565) when compared to single cells from the sham control [Figure 1G, H].

Principal component analysis (PCA) of the cumulative data revealed how strongly each wavelength influences a principal component (PC). The PCA biplot suggests that the photonic profile at λ565 had a significant influence on the PC1 components [Figure 1I]. PCA biplots also revealed how each wavelength correlated with one another. The smaller angle implies a positive correlation whereas a larger angle suggests a negative correlation. The photonic

profile at λ565 had significant divergence from other variables suggesting that this variable was poorly correlated with other wavelengths [Figure 1J]. Linear discriminant analysis (LDA) revealed that single cells from sham and ligated vessels could be easily separated across the five wavelengths [Figure 1K]. Confusion matrices revealed that 88% of the sham cells were similar to each other with only a small proportion of cells classified as similar to cells from ligated vessels [Figure 1L]. In contrast, 21% of ligated cells were classified as similar to sham cells with an accuracy of 86.2% on a cross-validated leave-one-out basis [Figure 1L].

Taken together, these results reveal that the single-cell autofluorescence emissions across five wavelengths *ex vivo* are of sufficient coverage, specificity and overall quality to unambiguously identify the majority of carotid artery cells from sham vessels as differentiated Myh11^{+}, SMA $^{+}$ contractile SMCs. However, in ligated vessels, PCA analysis revealed that the majority of cells exhibit a unique spectral profile with a minority of cells similar to differentiated sham SMCs *ex vivo.*

Single cell photonics of B-cells and macrophages *in vitro*

Single cell photonic measurements were recorded in human B lymphocytes (Ramos B) and murine macrophages (J774A.1) in 110 cells across the same five wavelengths using a centrifugal LoaD platform and the cells visualised by phase contrast microscopy on each V-cup [Suppl Figure 1A]. PCA analysis of 55 cells/group demonstrated that single cells clustered tightly and away from each other [Suppl Figure 1B] while LDA analysis confirmed that both cell types could be easily separated from each other [Suppl Figure 1C].

The photonic intensity of both cell types was also compared to cells from sham and ligated vessels [Figure 2A-D]. PCA and LDA analysis confirmed that both cell types clustered away from sham and ligated cells [Figure 2E] and were easily separated from each other [Figure 2F]. Confusion matrices revealed a 100% separation between Ramos B and J774A.1 cells and also successfully discriminated sham cells and ligated cells from J774A.1 and Ramos B cells, with an accuracy of 79.2% on a cross-validated leave-one-out basis [Figure 2G].

Taken together, these results suggest that the single-cell photonics identifies Ramos B and J774A.1 cells as distinct cell populations that are clearly different to isolated cells of sham and ligated vessels.

Single cell photonics of aortic SMCs ex vivo and cultured SMCs

In order to establish if differentiated SMCs differ in their photonic profile from de-differentiated SMCs in culture, single cell autofluorescence emissions were also recorded in freshly isolated aortic SMCs *ex vivo* and Movas SMCs in culture across five wavelengths using a centrifugal LoaD platform. The cells were visualised by phase contrast microscopy on each V-cup [Suppl Figure 2A] and their photonic profile recorded [Figure 3A]. PCA analysis demonstrated that a fraction of Movas SMC clustered towards aortic SMCs [Suppl Figure 2B] while LDA analysis confirmed a proportion of Movas SMC were similar to aortic SMCs [Suppl Figure 2C]. Both cell types had lower photonic intensities across each wavelength when compared to Ramos B cells [Figure 3B] and were also easily separated by LDA on a cross-validated leave-one-out basis with 87.8% accuracy [Figure 3C].

In order to establish if differentiated SMCs differ between vascular beds (aortic vs carotid), the photonic profile of aortic SMCs *ex vivo* and aortic Movas SMC in culture were compared to cells isolated from the carotid artery *ex vivo.* Aortic SMCs *ex vivo* and Movas SMC were similar across most wavelengths [Figure 3D, E] and clustered towards each other and cells from sham vessels [Suppl Figure 2D, F, H, J]. In contrast, they exhibited lower photonic intensities [Figure 3G,H] and clustered away from cells isolated of ligated vessels [Suppl Figure 2H, J]. LDA analysis confirmed that both cell types were similar to cells from sham vessels [Suppl Figure 2E, G, I] but distinct from cells isolated from ligated vessels [Figure 3F, Suppl Figure F, J K]. Confusion matrices successfully classified cultured aortic SMCs *ex vivo* and further suggested that Movas SMC shared similarities with aortic SMCs. Moreover, while a proportion of cells isolated from sham vessels were similar to Movas SMCs (26%) and aortic SMCs (6%), respectively, the majority of cells from ligated vessels were distinct with an accuracy of 72% on a cross-validated leave-one-out basis [Figure 3L].

Taken together, single-cell photonics clearly identifies similarities between cultured Movas SMCs and aortic SMCs cells *ex vivo*. Despite the fact that freshly isolated differentiated aortic SMCs and carotid artery SMCs from sham vessels *ex vivo* enrich for contractile markers (SMA and Myh11), these cells could still be separated based on their photonic profile. Moreover, only a small population of cells from ligated vessels (<3%) were classified as similar to Movas SMC and aortic SMCs *ex vivo.*

Single cell photonics of bone marrow-derived mesenchymal stem cells and their myogenic progeny.

In order to establish if single cell autofluorescence emissions across five broadband light wavelengths could discriminate undifferentiated stem cells from their myogenic progeny, we next examined single cell photonics of bone marrow-derived mesenchymal stems (MSCs) and their myogenic SMC progeny following stimulation with media supplemented with TGF-β1. Stem cells were first directly compared for differences using conventional genetic, biochemical and immunohistochemical analysis before and after myogenic differentiation with TGF-β1 [Figure 4A-D]. Bone marrow-derived MSCs were treated with or without TGF-β1 (2ng/mL) for 7 days before the expression of SMC differentiation markers, calponin 1 (Cnn1) and myosin heavy chain 11 (Myh11) was assessed by immunohistochemistry [Figure 4A]. There was a significant increase in the fraction of Cnn1 and Myh11 positive cells in TGF-β1 treated cells [Figure 4B] concomitant with a significant increase in the enrichment of the SMC epigenetic histone mark, di-methylation of lysine 3 on Histone 4 (H3K4me2) [39] and a decrease in the repressive mark, tri-methylation of lysine 27 on Histone 3 (H3K27me3)[50] at the Myh11 locus [Figure 4C]. The expression of Cnn1 and Myh11 was also increased in protein lysates following with TGF-β1 treatment [Figure 4D].

Single cell autofluorescence emission photonic measurements were recorded in MSCs across five wavelengths before and after TGF-β1 treatment for 7, 14 and 28 days, respectively, using the centrifugal LoaD platform. The cells were visualised by phase contrast microscopy on each V-cup [Suppl Figure 3A]. Their photonic profile was compared [Figure 4E-G] and PCA analysis revealed that MSCs clustered tightly and away from their myogenic progeny following differentiation over time [Suppl Figure 3B, D, F]. LDA analysis also indicated that

undifferentiated MSCs could be easily separated from their myogenic progeny after 7, 14 and 28 d, respectively [Suppl Figure 3C, E, G]. PCA analysis of each group revealed that MSCs and their myogenic progeny cluster away from each other [Suppl Figure 3H] while LDA analysis confirmed that MSCs and their myogenic progeny could be easily separated [Figure 4H]. Confusion matrices successfully classified MSCs and all their myogenic progeny with an accuracy of 96.3% on a cross-validated leave-one-out basis [Suppl Figure 3I].

In order to establish if undifferentiated MSCs or their TGF-β1-induced myogenic progeny share spectral similarities with cells isolated from sham and ligated vessels *ex vivo,* their photonic profiles were compared across the five wavelengths. The photonic intensity of undifferentiated MSCs was significantly lower than cells from sham vessels [Figure 4I] but increased when these cells were treated with TGF-β1 for 28d [Figure 4J]. The photonic intensity of MSC-derived myogenic progeny after 28d was significantly higher at λ630 and λ670 nm when compared to cells from ligated vessels [Figure 4K]. PCA analysis demonstrated a clear separation between MSC-derived myogenic progeny (after 14 and 28d) and cells from sham and ligated vessels, while undifferentiated MSCs and their myogenic progeny after 7 d clustered towards cells from sham vessels [Figure 4l]. LDA analysis confirmed that MSC-derived myogenic progeny could be separated from cells of ligated vessels but shared some similarities with cells of sham vessels [Figure 4M]. To confirm that the increased photonic intensity following TGF-β1 treatment of MSCs was not due to the inductive stimulus itself, Ramos B cells were also treated with TGF-β1 for 7 days before single cell photonics across all wavelengths was assessed. TGF-β1-treated Ramos B cells had lower photonic intensities across all wavelengths, including at λ565 nm wavelength [Figure 4N]. Confusion matrices classified 27% of cells from sham vessels and 3% of cells from ligated vessels as similar to MSCs treated with TGF-β1, on a cross-validated leave-one-out basis with 79.1% accuracy [Figure 4O].

The single cell photonic profile of MSCs and their myogenic progeny was also compared to Ramos B cells, J774A.1 cells, aortic SMC and Movas SMCs [Suppl Figure 4]. PCA and LDA analysis confirmed that MSCs and their myogenic progeny clustered away from Ramos B cells and could be easily separated while MSCs and their progeny after 7d clustered towards J774A.1 cells [Suppl Figure 4A, B]. Confusion matrices confirmed that 21% of J774A.1 cells

were classified similar to MSCs and their myogenic progeny on a cross-validated leave-one-out basis with 92.8% accuracy [Suppl Figure 4E]. In a similar manner, PCA and LDA analysis revealed that MSCs and their myogenic progeny after 7d clustered towards aortic SMCs and cultured Movas SMCs [Suppl Figure 4C, D], consistent with trans-differentiation of macrophages to SMCs (Ninomiya et al., 2006). Confusion matrices classified 16% of Movas SMCs and 20% of aortic SMCs as similar to MSCs and their myogenic progeny on a cross-validated leave-one-out basis with 80.1% accuracy [Suppl Figure 4F].

Taken together, these results suggest that single-cell photonics clearly discriminates MSCs from their myogenic progeny. Moreover, while SMCs isolated from sham vessels, aortic SMCs and Movas SMCs share some similarity with MSC-derived myogenic progeny, the photonic profile of the majority of cells isolated from ligated vessels (bar those MSC-derived progeny that resemble cells from sham vessels, aortic SMCs and Movas SMCs) was distinct *ex vivo.*

Single cell photonics of C3H/10T1/2 mesenchymal stem cells and their myogenic progeny

In a similar manner, we next examined whether single cell photonics could discriminate undifferentiated C3H/10T1/2 mesenchymal stem cells from their TGF-β1- induced myogenic progeny. Myogenic differentiation of C3H/10T1/2 stem cells was confirmed by conventional genetic, biochemical and immunohistochemical analysis before and after myogenic differentiation with TGF-β1 [Figure 5A-D]. Immunocytochemical analysis of the expression of SMC differentiation markers, Cnn1 and Myh11 confirmed myogenic differentiation of these cells in response to TGF-β1 [Figure 5A]. There was a significant increase in the fraction of Cnn1 and Myh11 positive cells in TGF-β1 treated cultures [Figure 5B] concomitant with a significant increase in Cnn1 and Myh11 expression in protein lysates [Figure 5C] and Cnn1 mRNA levels [Figure 5D].

Single cell photonic measurements were recorded across five wavelengths in C3H/10T1/2 cells before and after TGF-β1 treatment for 7 days using the centrifugal LoaD platform and were visualised by phase contrast microscopy on each V-cup [Suppl Figure 5A]. Their photonic profile was compared [Figure 5E] and PCA analysis demonstrated that undifferentiated C3H/10T1/2 cells clustered tightly and away from both their myogenic progeny [Figure 5F]

and Ramos B cells and J774A.1 cells [Figure 5G]. LDA analysis confirmed that C3H/10T1/2 cells and their myogenic progeny could be easily separated on a cross-validated leave-one-out basis with 99.3% accuracy [Figure 5H].

The photonic intensity of C3H/10T1/2 derived myogenic progeny was also compared to cells isolated from sham and ligated vessels [Figure 5I, J]. PCA analysis demonstrated that C3H/10T1/2 cells and their myogenic progeny clustered away from isolated cells of ligated vessels, but towards isolated cells of sham vessels [Figure 5K]. LDA analysis confirmed that C3H/10T1/2 cells and their myogenic progeny could be separated from cells isolated from ligated vessels [Figure 5L]. Confusion matrices classified 33% of cells isolated from sham vessels and 2% from ligated vessels as similar to C3H/10T1/2 cells and their myogenic progeny on a cross-validated leave-one-out basis with 75.1% accuracy [Figure 5M].

Single cell photonics of C3H/10T1/2 cells and their myogenic progeny were also compared to aortic SMC and Movas SMCs. PCA and LDA analysis confirmed that C3H/10 T1/2 derived myogenic progeny clustered towards aortic SMC and Movas SMCs [Suppl Figure 5C, D]. Confusion matrices classified 25% of Movas SMC cells and 22% of aortic SMCs as similar to C3H/10T1/2 cell-derived myogenic progeny on a cross-validated leave-one-out basis with 78.2% accuracy [Suppl Figure 5G]. In a similar manner, PCA and LDA analysis confirmed that MSC-derived myogenic progeny clustered towards C3H/10T1/2 cells and their myogenic progeny [Suppl Figure 5E, F]. Confusion matrices classified 4% of MSCs and 9% of MSC-derived myogenic progeny as similar to C3H/10T1/2 cells [Suppl Figure 5H]. Approximately 12% of MSCs and 21% their myogenic progeny were classified as similar to C3H/10T1/2 derived progeny, respectively, on a cross-validated leave-one-out basis with 88.5% accuracy [Suppl Figure 5H].

Taken together, these results suggest that single-cell photonics clearly discriminate C3H/10T1/2 mesenchymal cells from their myogenic progeny. Moreover, while cells isolated from sham vessels share significant similarity with C3H/10T1/2-derived myogenic progeny, the photonic profile of the majority of cells isolated from ligated vessels (bar those C3H/10T1/2-derived progeny that resemble cells from sham vessels) were distinct *ex vivo.*

Lineage Tracing analysis of perivascular S100β$^+$ vascular stem cells in normal (sham) and (ligated) injured vessels following flow restriction.

In order to determine the source of medial and intimal cells following flow restriction, lineage tracing analysis was performed using transgenic *S100β-eGFP-CreERT2-Rosa-26-tdTomato* reporter mice [Figure 6A]. As cre-mediated recombination results in a permanent heritable change in a cell's genome, these cells and their progeny remain tdTomato positive (tdT$^+$). The animals were treated with tamoxifen (Tm) for 7 days to induce nuclear translocation of CreER(Tm) and subsequent recombination to indelibly mark resident S100β$^+$ mVSc with red fluorescent tdTomato four weeks prior to flow restriction [Figure 6B]. Only S100β$^+$ mVSc cells present during the period of Tm treatment are marked with tdT and tracked. Morphometric analysis of the *S100β-eGFP-CreERT2-Rosa-26-tdTomato* mice confirmed significant intimal thickening in the LCA compared to the contralateral right carotid artery (RCA) in transgenic mice following flow restriction for 21 days [Figure 6C].

The tissue specificity and recombination efficiency of the Tm-induced Cre activity was confirmed in bone-marrow smears and neuronal tissue from *S100β-eGFP-CreERT2-Rosa-26-tdTomato* mice. Treatment with Tm resulted in Cre-mediated recombination and expression of S100β- tdT in >90% of neuronal cells of the carotid sinus nerve Hering's nerve without any S100β-tdT$^+$ cells observed in the bone marrow smears [data not shown]. The neuronal staining was confirmed by immunohistochemical analysis of S100β expression using both anti-S100β and anti-tdT antibodies, in addition to S100β-eGFP and S100β-tdT staining within these neuronal cells [data not shown].

Treatment of *S100β-eGFP-creER2-Rosa26tdT* transgenic mice with Tm indelibly marked S100β$^+$ cells (S100β-tdT$^+$) within the adventitial layer of the LCA prior to flow restriction [Figure 6D]. No cells are marked when these double transgenic mice were treated with the vehicle control Corn oil) [Figure 6D]. Importantly, no S100β-tdT$^+$ cells were observed in the intimal (EC) or medial (SMC) layers of vessels following tamoxifen treatment before flow restriction [Figure 6D]. However, following ligation, there was a striking increase in the number of S100β-tdT marked cells within the medial and intimal layers of the ligated LCA, compared to RCA control [Figure 6E]. Cumulative analysis confirmed a significant increase in

the number [Figure 6F] and the fraction of S100β-eGFP$^+$ cells within the LCA medial and intimal layers, compared to the RCA control [Figure 6G]. Moreover a significant proportion (~40%) of these cells originated from an S100β-tdT marked parent population [Figure 6H]. Since intimal and medial cells are not marked with S100β-CreER tdT prior to injury, taken together, these data suggest that a significant proportion of intimal and medial cells are derived from a non-SMC S100β$^+$ parent population following flow restriction *in vivo.*

Single cell photonics of S100β$^+$ resident vascular stem cells and their myogenic progeny

In order to establish if single cell autofluorescence emissions could also discriminate these undifferentiated S100β$^+$ mVSc from their myogenic progeny *in vitro*, we next examined single cell photonics of S100β$^+$ mVSc before and after stimulation with media supplemented with TGF-β1, Jag1 (Notch ligand) or sonic hedgehog (SHh). Resident S100β$^+$ mVSc were first isolated from murine aorta by sequential plating. Immunocytochemical analysis confirmed that the cells were S100β positive [Suppl Figure 6A]. Myogenic differentiation of S100β$^+$ mVSc was confirmed by immunocytochemical analysis of Cnn1 expression, Cnn1 mRNA levels and enrichment of stable SMC epigenetic H3K4me2 histone mark at the Myh11 promoter before and after treatment of cells for 7 d with media supplemented with either TGF-β1 (2ng/mL), Jag1 (1.0µg/mL) or SHh (0.5µg/mL) [Figure 7A-D]. The fraction of Cnn1 positive cells increased in all treated cultures [Figure 7A, B] concomitant with a significant increase in Cnn1 mRNA levels [Figure 7C] and enrichment of H3K4me2 at the Myh11 locus [Figure 7D].

Single cell photonic measurements were recorded from individual S100β$^+$ mVSc captured on V-cups using a centrifugal LoaD platform and visualised by phase contrast microscopy on each V-cup [Suppl Figure 6B]. Myogenic differentiation was induced with media supplemented with either TGF-β1 (2ng/mL), Jag1 (1.0µg/mL) or SHh (0.5µg/mL), respectively for 14 d [Figure 7E-G]. The photonic intensity of the λ565 ± 20 nm wavelength increased in response to all three myogenic inducers while PCA analysis revealed that S100β$^+$ mVSc clustered away from their myogenic progeny following differentiation [Figure 7H-J]. LDA analysis confirmed that undifferentiated S100β$^+$ mVSc could be separated from their respective myogenic progeny on a cross-validated leave-one-out basis (TGF-β1:77.1%, Jag-1: 90% and SHh: 93.4% accuracy)

[Figure 7K-M]. PCA and LDA analysis of the combined data confirmed S100β$^+$ mVSc clustered away from their myogenic progeny following differentiation after 14 d [Figure N,O]. Confusion matrices successfully classified S100β$^+$ mVSc and their myogenic progeny when cross-validated on a leave-one-out basis with 79.5% accuracy [Figure 7P].

The photonic intensities of individual S100β$^+$ mVSc were then compared to freshly isolated aortic SMC *ex vivo* and cultured Movas SMCs. S100β$^+$ mVSc and their myogenic progeny clustered away from aortic SMC and Movas SMCs [Suppl Figure 6C] while LDA analysis revealed that these cells could be easily separated from SMCs [Suppl Figure 6D]. Confusion matrices classified Movas SMCs and aortic SMCs as distinct cell populations from S100β$^+$ mVSc and their myogenic progeny on a cross-validated leave-one-out basis with 76.3% accuracy [Suppl Figure 6E]. Similarly, PCA and LDA analysis confirmed that S100β$^+$ mVSc and their myogenic progeny clustered away from J774A.1 and Ramos B cells, respectively, and are also easily discriminated [Suppl Figure 6F, G]. Confusion matrices classified J774A.1 and Ramos B cells as distinct on a cross-validated leave-one-out basis with 85.7% accuracy [Suppl Figure 6H]. The photonic intensities of individual S100β$^+$ mVSc were also compared to MSCs and their myogenic progeny. S100β$^+$ mVSc and their myogenic progeny also clustered away these cells [Suppl Figure 7A] while LDA analysis revealed that they could be easily separated from each other [Suppl Figure 7B]. Confusion matrices classified mVSc and MSCs as distinct cell populations in addition to their myogenic progeny on a cross-validated leave-one-out basis with 88.3% accuracy [Suppl Figure 7C].

In order to establish if undifferentiated resident S100β$^+$ vSC or their myogenic progeny share spectral similarities with cells isolated from normal and injured vessels *ex vivo, t*he photonic intensity of undifferentiated S100β$^+$ mVSc and their myogenic progeny was compared to cells isolated from sham [Figure 8A-C] and ligated vessels [Figure 8D-F]. PCA analysis revealed that S100β$^+$ mVSc and their TGF-β1-, Jag1- and SHh-derived myogenic progeny clustered away from sham cells [Figure 8G] but towards isolated cells of ligated vessels [Figure 8G]. LDA analysis demonstrated that these cells were separated from cells of sham vessels but were not as easily separated from cells of ligated vessels [Figure 8H]. Confusion matrices revealed that 15% of cells isolated from sham vessels were classified as similar to TGF-β1-derived myogenic progeny [Figure 8I, J], while 21% of cells from ligated vessels were classified as

S100β$^+$ mVSc and their myogenic progeny, on a cross-validated leave-one-out basis with 73.9% accuracy [Figure 8I, K].

Single cell photonics identifies S100β$^+$ resident vascular stem cells and their myogenic progeny within ligated vessels

In order to assess the contribution of S100β$^+$ mVSc and their myogenic progeny to the overall heterogenous phenotype of cells isolated from sham and ligated vessels, the photonic autofluorescence emission profiles of (i) Movas SMCs, (ii) aortic SMCs and (iii) S100β$^+$ mVSc and their myogenic progeny were used as part of a training set before sham and ligated cells were interrogated against this trained dataset using LDA. The dataset consisted of 685 cells whose measurements spanned across 5 wavelengths. The spectral data was normalised by dividing by the background photonic intensity at each wavelength before the dimensionality of the log2 fold changes were pre-processed through a Multiclass Fisher's Linear Discriminant Analysis (Multiclass FLDA) filter, as previously described using WEKA machine learning tool kit [52] and further analysed by LDA using PAST4 [53]. LDA analysis separated each group on a cross-validated leave-one-out basis with 66.7 % accuracy. In sham vessels, the majority of cells were classified as Movas SMC [Figure 8L]. In contrast, the majority of cells within ligated vessels were classified as S100β$^+$ mVSc or their myogenic progeny (~65%) with the remainder classified as Movas SMC [Figure 8M]. When cells isolated from sham vessels were also included in this training set, the majority of sham cells were classified as SMC (either sham, Movas or aortic SMCs) [Figure 8N]. In contrast, in ligated vessels, the majority of cells were classified as S100β$^+$ mVSc and their myogenic progeny on a cross-validated leave-one-out basis with 66.6% accuracy. Taken together, these data suggest that a significant proportion of ligated cells within injured vessels share a photonic profile similar to S100β$^+$ mVSc and their myogenic progeny [Figure 8P].

Finally, in order to assess the contribution of all cell types to the overall heterogenous phenotype of cells isolated from ligated vessels, the photonic profiles of (i) isolated cells from sham vessels, (ii) de-differentiated Movas SMCs (iii) S100β$^+$ mVSc and their myogenic progeny, (iv) MSCs and their myogenic progeny (v) Ramos B cells and (vi) J774A.1 macrophages were again analysed by LDA as part of a an overall training set before single

cells isolated from ligated vessels were interrogated. The dataset consisted of 1063 cells whose measurements spanned across the 5 wavelengths. LDA analysis separated each group on a cross-validated leave-one-out basis with 67.7% accuracy [Figure 9A]. The majority of cells isolated from sham vessels were classified as themselves or Movas SMC, MSCs or their TGF-β1 derived myogenic progeny and compromised ~86% of all cells [Figure 9B]. When individual cells isolated from ligated vessels were interrogated against this trained dataset, a significant number of ligated cells were classified as S100β^{+} mVSc and their TGF-β1-, Jag1- and SHh-derived myogenic progeny [Figure 9C].

These data suggest that single-cell photonic profiles *ex vivo* are of sufficient coverage, specificity and overall quality for LDA algorithms to discriminate various different cell types within injured vessels *ex vivo.* The data also reveal that a significant number of ligated cells were classified as S100β^{+} mVSc and their myogenic progeny *in vitro* [Figure 9D]. Taken together, these data suggest that a significant number of ligated cells *ex vivo* share a photonic profile similar to S100β^{+} mVSc and their TGF-β1-, Jag1- and SHh-derived myogenic progeny *in vitro*.

Supervised machine learning to interrogate isolated cells from normal and injured vessels

As part of a supervised machine learning procedure, we employed MLP artificial neural network analysis to further classify each cell population and interrogate cells from sham and ligated vessels. It's the simplest and most commonly used neural network architecture due to its structural flexibility, good representational capabilities and availability of a large number of training algorithms [48]. Cells were first classified to create a ground truth for each sample before the data were normalized to one by dividing the fluorescence intensity at each wavelength by the average background intensity at that wavelength. Dimensionality reduction was achieved through Multiclass FLDA filter before MLP neural network analysis with 2 hidden layers was performed using the WEKA machine learning tool kit [52] [Figure 10A]. The dataset consisted of 1008 cells whose measurements spanned across the 5 wavelengths. To train the network, we optimized several experimental conditions, including number of wavelengths for input data, number of hidden layers, the momentum and learning rate. The final classification model had an F-score of 0.928, recall of 0.929 and precision score of 0.929.

Cross validation confirmed that optimized neural networks can identify all cell types with high performance, based only on their autofluorescence emissions and resulted in an F-score of 0.81. The cells were also trained on a 66 % split before the remainder was tested and the F score dropped to 0.77. This trained data set was subsequently used to interrogate photonic datasets of cells isolated from sham and ligated vessels *ex vivo.* The majority of sham cells (>80%) were classified as sham [Figure 10C]. In contrast, ~50% of ligated cells were classified as mVSc and their SHh-derived myogenic progeny in addition to sham cells (~19%) and non-classified ligated cells [Figure 10C].

Taken together, supervised machine learning using MLPs neural network analysis successfully identified each cell type in the training set with >90% accuracy and further suggests that a significant number of ligated cells *ex vivo* are classified as S100β$^+$ mVSc and their myogenic progeny *in vitro* [Figure 10D].

Elastin and Coll 3A1 contribute to the photonic intensity of stem cell-derived myogenic progeny at λ565 ± 20 nm wavelength.

PCA loading plots of cells isolated from sham and ligated vessels suggest that the photonic differences at λ565 ± 20nm had a significant influence on PC1 [Figure 1I]. Similarly, the photonic profile at λ565 ± 20nm had a significant influence on PC1 in PCA biplots of single MSCs, S100β$^+$ mVSc and C3H/10T1/2 cells following myogenic differentiation *in vitro* when compared [Figure 11A]. When the photonics of single cells isolated from sham and ligated vessels was compared to MSCs, S100β$^+$ mVSc and C3H/10T1/2 cells at λ565 ± 20nm, there was a clear increase in the intensity at this wavelength in cells isolated from ligated vessels and cells undergoing myogenic differentiation [Figure 11B]. In order to identify the fluorophores that may contribute to the increase in the photonic intensity of stem cell-derived myogenic progeny at λ565 ± 20 nm, the roles of two important auto fluorescent molecules, elastin and Coll3A1 were assessed [42]. The mRNA levels of elastin and Coll3A1 were both significantly increased following myogenic differentiation of mMSCs with TGF-β1 treatment [Figure 11C] and S100β$^+$ mVSc with TGF-β1 [Figure 11D] and Jag1 [Figure 11E]. The effects of elastin and Coll3A1 depletion on the photonic profile of undifferentiated mMSCs at

the λ565 ± 20 nm wavelength was also assessed following transfection of cells with specific siRNA duplexes targeting elastin and Coll3A1transcripts, respectively. A fluorescently tagged siRNA was used to validate transfection efficiency at over 80% [data not shown] before elastin and Coll3A1 mRNA depletion following TGF-β1 treatment was confirmed by qRT-PCR after 72 h [Figure 11F]. The photonic intensity of undifferentiated cells at λ565 ± 20nm following Coll3A1 depletion was significantly decreased without a significant effect following elastin depletion, when compared to the scrambled siRNA controls [Figure 11G]. However, the photonic intensity at λ565 ± 20 nm was significantly reduced following treatment with TGF-β1 for 7 d in both elastin and Coll3A1 depleted mMSCs [Figure 11G].

These data suggest that the autofluorescence emissions at λ565 ± 20nm during myogenic differentiation of undifferentiated stem cells was due, in part to changes in elastin an Coll3A1 expression within these cells.

Discussion

A hallmark of vascular pathology is the presence of neointimal SMC-like cells within adaptive lesions [14]. Endothelial dysfunction due to changes in blood flow and shear stress precedes the appearance of adaptive lesions and is considered a pivotal event in the development of subclinical atherosclerosis [3]. Herein, we combine single cell label-free autofluorescence photonic emissions *ex vivo* with lineage tracing analysis of S100β$^+$ mVSc *in vivo* to examine the cellular heterogeneity of vascular lesions following iatrogenic flow restriction. We clearly demonstrate that single cell photonics across five wavelengths *ex vivo* is of sufficient coverage, specificity and quality to discriminate undifferentiated stem cells from their myogenic progeny *in vitro.* Moreover, these photonic datasets can classify aortic and carotid medial SMCs from each other *ex vivo* and efficiently discriminate these cells from undifferentiated MSCs, undifferentiated resident S100β mVSc, B-cells and macrophages *in vitro*. We further provide experimental evidence that upregulation of Coll 3A1 and elastin is a hallmark of undifferentiated stem cells undergoing myogenic differentiation *in vitro* and contributes to the changes in the photonic signature of carotid artery cells at λ565 nm following injury. Using LDA training of these datasets in combination with cell fate mapping of S100β$^+$ mVSc *in vivo,* we confirm that a substantial number of cells present within injured vessels are S100β$^+$ mVSc and their myogenic progeny. Finally, supervised machine learning using MLP neural network analysis successfully discriminated each cell type *ex vivo* and *in vitro* and further suggested that a substantial number of cells within injured vessels following flow restriction are similar to S100β$^+$ mVSc and their SHh-derived myogenic progeny when interrogated against this trained dataset.

The major objective of this study was to determine whether a single cell label-free optical multi-parameter interrogation platform [LiPhos: Living Photonics: Monitoring light propagation through cells] could discriminate various cell phenotypes *ex vivo.* We clearly demonstrate that single SMC cells from aortic and carotid vessels display significant differences in their specific autofluorescence emissions across the five wavelengths. Based on these data, we conclude there is considerable heterogeneity in the photonic profile of medial SMCs between vascular beds in healthy animals, and yet find that medial SMCs uniformly express SMC contractile markers (SMA and Myh11). Similar conclusions were

observed for medial SMCs from various vascular beds of healthy animals using scRNA-seq data as a discriminator [21]. Carotid artery SMCs are atheroprone and are derived from the neural crest [54] whereas medial SMCs from the thoracic aortic are of somatic mesoderm origin [55] and are considered atheroresistant. While single-cell photonics identified some similarities between sub-cultured de-differentiated aortic Movas SMCs, aortic SMCs and cells isolated from sham vessels *ex vivo*, these cells could still be discriminated from each other across the five wavelengths by LDA. This heterogeneity is noteworthy as it may indicate the existence of specific subsets of medial SMCs with particular disease-relevant photonic profiles. The sources of this heterogeneity may include their embryologic origin (neuroectoderm vs mesoderm) or differences in their respective microenvironments.

Bone-marrow derived MSCs (BM-MSCs) and C3H/10T1/2 cells are considered good models of SMC differentiation from mesoderm precursors *in vitro* [56,57] and single cell autofluorescence emissions clearly discriminated undifferentiated stem cells from their myogenic progeny. Indeed, we have previously demonstrated that stem cell-derived myogenic progeny share a similar photonic profile with 'de-differentiated' sub-cultured vascular SMCs *in vitro* using Raman and Fourier Transform Infrared (FTIR) spectroscopy [58]. It is also not surprising that their myogenic progeny following TGF-β1 stimulation shared similar photonic characteristics to mesoderm-derived aortic SMCs *ex vivo* and cultured Movas SMCs. However, they also shared spectral characteristics similar to neuroectoderm-derived carotid artery medial SMCs from healthy animals suggesting that C3H/10T1/2 cells and BM-MSCs may be capable of generating neuroectoderm derived lineages in response to TGF-β1. On the other hand, resident mVSc are neuroectoderm in origin and express neural stem cell markers such as S100β, Nestin, Sox10 and Sox17 [20,59–61]. It is unlikely these cells are derived from medial SMCs as they do not enrich for the stable SMC epigenetic histone mark, H3K4me2 at the Myh11 locus [39] but do acquire it following TGF-β1, Jag1 and SHh stimulation. These myogenic progeny shared some spectral similarity with cells isolated from healthy carotid arteries but were most notable for their similarity to cells of ligated vessels.

For many years, SMC-like cells within neointimal lesions have been considered monoclonal/ oligoclonal in origin arising from the expansion of a pre-existing resident clonal population of cells [62–65]. As a general rule, SMCs are purported to switch from a contractile phenotype to a

less mature synthetic phenotype following vascular injury [66]. This phenotypic switch is accompanied by loss of expression of SMC differentiation contractile markers, increased proliferation, and the synthesis and release of several signalling molecules including pro-inflammatory cytokines, chemotaxis-associated molecules, growth factors and extracellular matrix proteins [66]. Despite extensive research, their origin remains controversial [67]. In particular, whether these clonal progeny are derived primarily from differentiated medial SMCs [11,21,66], endothelial cells [20,68], and/or resident vascular stem cells (mVSc) [15,20,22,59,69,70]. Although the Myh11-CreERT2 transgene was originally deemed specific for vascular SMC [71], data indicating expression of this and other SMC differentiation genes in non-SMC populations has recently emerged raising the possibility that other resident cells may contribute to lesion formation [72–74].

In this study, we provide compelling genetic evidence using lineage tracing analysis that vascular lesions contain an abundance of S100β$^+$ cells that originate from a non-SMC perivascular S100β$^+$ parent population. Moreover, we confirm these observations using single cell photonics of S100β$^+$ vSCs and their myogenic progeny *in vitro* by comparing their photonic profile *in vitro* to the autofluorescence emissions from ligated cells following injury. When the photonic profile of a range of cells *in vitro* and *ex vivo* were deployed as part of a training set using LDA, a substantial proportion of cells within ligated vessels were classified as S100β$^+$ vSCs and their SHh-derived myogenic progeny. Several previous lines of evidence point to a role for Hh signalling in vascular lesion formation [30,75–80]. Adventitial Sca1$^+$ stem cells that co-localise with SHh and its receptor, Ptch1 [81] contribute to intimal thickening *in vivo* [77,82,83]. Moreover, while we have previously reported that local perivascular knockdown of the Ptch1 receptor attenuates intimal thickening [32], systemic inhibition of Hh signalling, using a smoothened inhibitor, also significantly decreases arterial Ptch1 and Gli expression concomitant with a reduction in Sca1$^+$ cells and lesion formation *in vivo* [84].

Deep learning, a form of machine learning, uses a multilayered neural network to mimic a human neural circuit structure [49]. It has become increasingly popular in finding latent data structures and classifying highly nonlinear datasets, attributes that are ideal for physical sciences and, more particularly, photonics [49]. Machine learning has also proven ideal for classifying cell subtypes from label-free images [85] to predict macrophage activation, [86] lymphocyte cell types, [87] pluripotent stem cell-derived endothelial cells [88] and differentiating

primary hematopoietic progenitors [89]. Our analysis using a pre-trained MLP neural network clearly demonstrated that supervised machine learning can be successfully deployed to classify cells from normal and injured vessels with autofluorescence intensity as the only input. Similarly, undifferentiated stem cells could be easily discriminated from their myogenic progeny using the same trained autofluorescence dataset. Using this MLP artificial neural network, we successfully classified sham and ligated cells *ex vivo* and predicted the presence of S100β^{+} mVSc and their progeny within injured vessels. These data support previous lineage tracing studies that mapped stem-cell derived myogenic progeny within vascular lesions [15–20]. Our success in classifying these cells without exogenous contrast agents suggests that modern machine learning approaches may help compensate for spectral data with less molecular specificity and may provide further insight into the function and regulation of stem cells and their progeny in disease. Our study also highlights how photonics might be deployed for functional testing of undifferentiated stem cells and how they might respond to various inductive signals. This should facilitate the identification of corresponding plastic cell population(s) in human vessels for targeted therapy and diagnosis. Beyond the immediate findings of our study, these single-cell photonic profiles generated from healthy and injured vessels will enable further examination of vascular cell heterogeneity and function in disease.

The application of single cell autofluorescence to study of the vascular physiology is still emerging [90]. In this study, we clearly demonstrate that specific autofluorescence emissions from single cells *ex vivo* or *in vitro* can be detected label-free on a novel centrifugal microfluidic LoaD platform [47]. Mammalian cells are known to contain molecules which become fluorescent when excited by UV/Vis radiation of suitable wavelength arising from endogenous fluorophores [42]. Detection has greatly accelerated over the last decade in an effort to identify specific spectral differences between individual cells/tissues (Burger et al., 2015; Croce et al., 2018; King et al., 2019). Distinguishing different cell populations using label free single cell photonics has facilitated the development of new medical diagnostic tools for various disease conditions [92–94]. There are many endogenous fluorescence sources of contrast but the most robust and widely deployed have been those associated with metabolism and structural architecture [44]. These signatures contain significant information of diagnostic value and represent the sum of individual autofluorescence signals from all fluorophores within single cells. They offer the greatest impact when deployed in combination with clinical

assessment of normal, altered or diseased states and act as powerful intrinsic "optical antennas" of the morphological and functional properties of cells. They depend not only on the chemical nature of the endogenous fluorophores but also on concentration, chemical and physical state, supramolecular organization, aggregation phenomena, interaction with other fluorophores, microenvironment and tissue optical properties [42].

Changes in the autofluorescence emissions associated with reduced nicotinamide adenine dinucleotide (phosphate) (NAD(P)H) and flavin adenine dinucleotide (FAD) have been widely characterized following oxygen- or glucose-depletion within cells [95] and during differentiation of progenitor stem cells [96,97]. In stem cells, the autofluorescence signal is strongly dominated by cellular autofluorescence, for which NAD(P)H and FAD are the major contributors [96,97] while other fluorophores such as collagens and elastin are dominant in vascular tissue [98]. The relative proportions of these fluorophores in vascular tissue are expected to change in disease and may reflect the energetic and structural health of the vascular cells. For example, the autofluorescence signals from collagen are known to increase due vascular injury, while changes in metabolic pathways are likely to occur as result of mitochondrial and energetic dysfunction, which will affect the relative proportions of NADH and NAD^+ and, similarly, FADH2 and FAD [42]. While structural alterations are relatively straightforward to report, due to the high quantum yield of collagen and its long fluorescence lifetime, metabolic alterations can be challenging to interpret due to the multitude of metabolic pathways and fluorophore species involved [90].

In this context, single cells isolated from injured vessels *ex vivo* exhibit enhanced photonic emissions, particularly at λ565nm, when compared to differentiated medial SMCs from normal vessels. Moreover, undifferentiated stem cells *in vitro* increase their intensity of emissions at λ565nm concomitant with an increase in elastin and Coll 3A1 expression. Mature elastin is formed by cross-linking of its precursor, tropoelastin produced by medial SMCs and released to the extracellular space for cross-linking and elastin fibre formation mediated by lysyl oxidase and the helper proteins fibulin-4 or -5 [99]. Its formation is restricted primarily to fetal life and infancy with mature elastic fibers remaining throughout the entire lifespan. However, under certain circumstances, elastic fibers are degraded and fragmented with age and disease, leading to increased stiffness of the arterial wall [100]. Indeed, several pathological stimuli control elastogenesis in the progression of arteriosclerosis, similar to the

marked increase in elastin content during development [101]. Vascular cells produce elastin as part of their reaction to increased mechanical stress associated with arteriosclerotic disease progression [102,103]. Moreover, elastin content is significantly increased following carotid artery injury [104] and TGF-β1 synergistically enhances elastin matrix regeneration by SMCs [105]. While specific knockdown of elastin in undifferentiated stem cells did not result in any changes at the λ565nm, it did cause a significant decrease in the photonic intensity following TGF-β1 treatment suggesting that changes in elastin content may contribute to the enhanced emissions at this wavelength.

Elastin expression is normally turned off in adults while collagens are subsequently synthesized shifting the arterial wall toward a stiffer range of collagen fibers in response atherogenic stimuli [99]. Collagen is commonly described as extracellular, fibrous protein and its photonic emissions are generally associated with hydroxylysyl-pyridinoline and lysyl-pyridinoline groups that are affected by age-dependent polymerization of monomeric chains and cross links [99]. In the normal arterial wall, collagen type I and Coll 3A1 are the main collagens in the media and adventitia while arterial injury may alter the balance between these two types of collagen [106]. Indeed, enhanced Coll 3A1 expression has been specifically detected within human restenotic lesions [107] and stented coronary arteries and is accompanied by increased expression of TGF-β1 [108]. The deposition of Coll 3 was also recently identified in neointimal SMC-like cells in a rat carotid model using 18F-fluorodeoxyglucose (FDG positron emission tomography - PET) [109]. In agreement with others, our study confirms that undifferentiated stem cells undergoing myogenic differentiation increase their collagen production [102,105]. Specific knockdown of Col3A gene expression resulted in a significant decrease in the photonic intensity at λ565nm in undifferentiated stem cells. Moreover, Coll 3A1 depletion reduced the photonic intensity at λ565nm following TGF-β1 induced myogenic differentiation. Collectively, these data suggest that both elastin and Coll 3A1 content may contribute, in part, to the enhanced photonic signature at this wavelength in both stem cell-derived myogenic progeny *in vitro* and in cells isolated from ligated vessels following injury *ex vivo.*

Independent of structural changes, there is also recent evidence linking cell metabolism to transcriptional activity during differentiation/de-differentiation cycles. This can be simple direct binding of metabolites to nuclear receptors (lac repressor, retinoic acid receptors) or

metabolic enzymes that act as transcriptions factors to progressively more complex mechanisms involving hypoxia-inducible factors [110]. A metabolic phenotype has recently been reported following programming and lineage-specific differentiation of vascular progenitors [111–113]. Moreover, phenotypic switching of cultured SMCs from a quiescent, contractile phenotype to a motile, synthetic de-differentiated phenotype also involves dramatic variations in cell metabolism concomitant with changes in cell morphology and gene expression [114]. Indeed, recent studies have strongly implicated the mitochondrial protein Poldip2 (Polymerase Delta Interacting Protein 2) in controlling SMC differentiation through a mechanism that involves regulation of metabolism and proteostasis [115]. Poldip2 deficiency reduces the activity of the Krebs cycle and inhibits rates of oxidative metabolism while increasing rates of glycolytic activity in many different cell types, including vascular SMCs [114]. While heterozygous Poldip2 deletion has no obvious phenotype, mice are protected against neointimal formation following injury [116] underlying the importance of metabolism in disease progression. Therefore, it is possible that the changes in the photonic emissions from ligated cells may also involve alterations in the metabolic state of these cells, in particular, if these cells are de-differentiated SMCs and/or stem cell derived myogenic progeny. While challenging to interpret, future studies will attempt to illuminate the potential contribution of individual key fluorophores involved in cell metabolism in single cells *ex vivo* during disease progression.

In conclusion, we have demonstrated that a novel single cell label-free optical multi-parameter interrogation system can successfully discriminate 'normal' differentiated medial SMCs from arteriosclerotic SMC-like cells *ex vivo* following vascular injury. Moreover, single cell photonics discriminates undifferentiated stem cells from their myogenic progeny, particularly at the λ565 nm, that may reflect their differentiation state. Furthermore, the photonic profile of cells isolated from normal and injured vessels closely resemble that of S100β^{+} mVSc-derived myogenic progeny. Photonic elucidation of this new cellular source for generating SMC-like cells following injury expands our current understanding of vascular pathology and may represent an important therapeutic strategy for combating subclinical atherosclerosis. This novel label-free optical system may also provide a suitable platform to develop enabling technologies that detect early stage vascular changes within the vessel wall

and thereby facilitate intervention and treatment to improve vascular function and reduce the morbidity associated with CVD.

Methods

Biochip Device: The biochip design was based on cell sedimentation under stagnant flow conditions due to the application of centrifugal force into an array of V-shaped capturing elements (Figure 1E). The base (microfluidic inlets and V-cup array) section of the biochip was fabricated in PDMS (Sylgard 184, Dow Corning GmbH, Germany). Moulds for PDMS casting were surface micro-machined using SU8-3025 (Microchem, USA) for manufacturing the V-cup array and the reservoirs. The biochip middle layer (chip support holder) was manufactured using poly(methyl meth-acrylate) (PMMA) with a thin layer of pressure sensitive adhesive (PSA) attached to its base. A laser cutter (Epilog Zing Laser, Epilog, USA) defined the middle layer of the biochip. The chip substrate consisted of a standard borosilicate microscope slide which was bonded to the chip middle layer using PSA. This hybrid chip was then treated by air plasma (1000 mTorr) for 5 minutes and assembled with the PDMS base to complete the biochip (Burger et al., 2015). The fabrication method for the biochip ensured transparency and biocompatibility and was leak free and facilitated long term stability. The operating principles of the V-cup array have been described previously [45]. Briefly, the sedimentation takes place with the liquid bulk at rest to provide high capture efficiency. V-cups (13 µm diameter) staggered in an array of 47 x 24 cups which can thus trap up to 1128 individual cells. Additional trap and pillar based locations are also on the biochip to facilitate a sub-population of cells to be selected (via optical tweezers) and further single cell assays. Finally, a disc for holding three biochips and for mounting onto the centrifugal test stand was manufactured using 3D printing. The centrifugal test setup comprised a motor for spinning the microfluidic chips (4490H024B, Faulhaber micromotor SA, Switzerland), a synchronized camera for image acquisition during rotation (TXG14c, Baumer AG, Germany) coupled to a motorized 12x zoom lens (Navitar, USA) and a strobe light unit (Drelloscop 3244, Drello, Germany) as described previously (Burger et al., 2015; 2012). The system integration between the microfluidic and optical systems for SCA was performed using an in-built optical detection and imaging system on the centrifugal test stand. The optical module incorporated a laser tweezers to manipulate individual cells on disc using a 1-W, 1064-nm infrared laser (Roithner Lasertechnik, Austria). This laser was focused through a 40x oil immersion microscope objective (CZ Plan Neofluar 40x/1.3 OIL PH3, Zeiss, Germany) with a numerical aperture (NA) of 1.3. This setup allowed a working distance of 200 µm. This objective was mounted on a piezo driven Z-drive with a

travel range of 100 µm (Fast PIFOC® Piezo Nanofocusing Z-Drive, PI, Germany) for fine focusing. Additionally, the module included a high sensitivity cooled CCD camera (Sensicam qe, PCO, Germany) which utilizes the same optical path as the laser to facilitate particle handling and ac-quisition of bright-field and fluorescent images. Excitation was performed by a 250-W halo-gen lamp (KL 2500 LCD, Schott, Germany) with an enclosed filter wheel to allow both broad-band light (λ = 360 - 800 nm) and selected fluorescent excitation (filtered at excitation wave-lengths of 403 ± 32 nm, 492 ± 15 nm, 515 ± 25 nm, 572 ± 15 nm and 610 ± 32 nm) and emission wavelengths (emission filters are 465 ± 20 nm, 530 ± 20 nm, λ565 ± 20 nm and 630 ± 20 nm and 670 ± 20 nm). The module was mounted on a computer controlled X-Y stage (Qioptiq, Germany). Measurement of background photons assessed the contribution of the chip PDMS material and the surrounding liquid (cell media), on a fully primed empty chip. The images are acquired post capture when the cells settle into the capture V-cup region. The method of travel through the chip was sedimentation based and did not impact on the fluorescence emissions as the cells experience minimum shear force as they travel through the chip. Spin speed for the cells travelling through the chip is fixed at 10Hz for all experiments to reduce any instrumentation variations. Excitation (lamp power etc.) and image acquisition settings (exposure time, min and max values etc.) were fixed and uniform across all experiments. The effect of the width of the excitation (15-32 nm) using commercial filters fitted into the imaging system revealed that changing an excitation filter bandwidth by a small increments had little impact on fluorescence excitation. In all studies, the entire cell was selected as the region of interest (ROI) and the mean value across the entire cell is presented. The experimental volume fraction of the cell probed and the standard deviation across each cell, in each wavelength, was low (data not shown).

Biochip Preparation and Microfluidic Testing: The device was placed in vacuum prior to introducing the liquids for a minimum of 30 minutes ensure complete and bubble-free filling. The biochip was primed with the appropriate cell culture media formulation for the cell type under test via the loading chamber on the top right section of the biochip. After priming, cells were introduced via the loading chamber on the top left section of the biochip. All pumping was performed the centrifugal test stand and a 3D-printed chip holder which allows three biochips to be tested in parallel, thus significantly increasing the cell capture efficiency of the V-cup array system compared to common, flow-driven systems (Burger et al., 2015). Initial

cell capture tests were performed using 20-µm polystyrene beads to emulate cell behaviour before being repeated using cells. In all cases, the sedimentation in absence of flow led to significantly increased occupancy of the V-cups (≥ 95%) compared to common, flow-driven methods (data not shown).

Tamoxifen-induced genetic lineage tracing

S100β-CreER-Rosa26tdT mice (average weight 20g, 6-8 wks old) were injected IP with tamoxifen (Tm) dissolved in corn oil at 75 mg/kg for 5 consecutive days. Carotid artery ligation (partial, or complete), or sham operation, was performed at 4 weeks after the last injection of Tm. At the indicated time post-ligation or sham operation, anesthetized mice were perfusion fixed and carotid arteries harvested for analysis.

Histomorphometry

At specified times post-ligation, mice were anesthetized (ketamine/xylazine) and perfusion fixed with 4% paraformaldehyde in sodium phosphate buffer (pH 7.0). Fixed carotids were embedded in paraffin for sectioning. Starting at the carotid bifurcation landmark (single lumen) a series of cross-sections (10 x 5 µm) were made, every 200 µm through 2 mm length of carotid artery. Cross-sections were de-paraffinized, rehydrated in graded alcohols and stained with Verhoeff-Van Gieson stain for elastic laminae and imaged using a Nikon TE300 microscope equipped with a Spot RT digital camera (Diagnostic Instruments). Digitized images were analyzed using SPOT Advanced imaging software. Assuming a circular structure *in vivo*, the circumference of the lumen was used to calculate the lumen area, the intimal area was defined by the luminal surface and internal elastic lamina (IEL), the medial area was defined by the IEL and external elastic lamina (EEL), and the adventitial area was the area between the EEL and the outer edge, essentially as described by us previously [8,84].

Haematoxylin and Eosin Staining of Tissue

For murine vessels, paraffin rehydration was conducted at room temperature by immersing the slides in xylene for 20 minutes. The slides were then immersed in the following gradients of ethanol for 5 minutes respectively: 100 %, 90 %, 70 % and 50 % ethanol. The slides were then rinsed in distilled H_2O_2 before washing in 1x PBS for 10 minutes. The slides were stored

in 1x PBS until ready when they were immersed in Harris Haematoxylin at room temperature for 8 min.

Immunofluorescent Staining of tissues.

Immunostaining essentially as previously described [8,78,84]. Carotid artery cryosections were air-dried for 1 h at room temperature, followed by incubation with blocking buffer (5% donkey serum, 0.1% Triton X-100 in PBS) for 30 minutes at room temperature and then incubated with primary antibody overnight at 4^0C in antibody solution (2.5% BSA, 0.3M Glycine and 1% Tween in DPBS). Murine and human arterial sections were stained with primary antibodies [Supplementary Table I]. Isotype IgG control and secondary antibody only controls were performed. For antigen retrieval, slides were brought to a boil in 10 mM sodium citrate (pH 6.0) then maintained at a sub-boiling temperature for 10 minutes. Slides were cooled on the bench-top for 30 minutes then washed in deionized water (3x5 min) each before being washed in PBS (3x5 min). The antigen retrieval protocol diminishes endogenous eGFP and Tdt tomato transgene signals. Therefore, those sections were co-stained with anti-eGFP antibody and anti-Td tomato antibody [Supplementary Table I].

For immunofluorescence staining, 5 consecutive images were obtained and processed using ImageJ software™ to analyze the collected images. Images were merged using the Image color-merge channels function. Merged signals and split channels were used to delineate the signals at single-cell resolution. Settings were fixed at the beginning of both acquisition and analysis steps and were unchanged. Brightness and contrast were lightly adjusted after merging.

Immunocytofluorescent staining of cells

Cells seeded onto UV sterilized coverslips were fixed with 3.7 % formaldehyde, (15 min, RT). If cells required permeabilization for the detection of intracellular antigens, cells were incubated in 0.025 % Triton X-100 PBS (room temp, 15 min). All coverslips were blocked (1 hr, RT) using 5 % BSA, 0.3 M Glycine, 1 % Tween PBS solution (1 hr, RT). Cells were incubated overnight with primary antibodies at 4^0C [Supplemental Table II], then washed twice with PBS to remove any unbound primary antibody before being incubated (1 hr, RT) with the recommended concentration of fluorochrome-conjugated secondary antibodies diluted in

blocking buffer [Supplementary Table II]. Following 2x wash in PBS, cell nuclei were stained using DAPI: PBS (dilution 1:1000) (15 min, RT). For each primary and secondary antibody used, a secondary control and an IgG isotype control was performed to assess nonspecific binding. An Olympus CK30 microscope and FCell™ software was used to capture images. Images were analysed using ImageJ software as described above. Settings were fixed at the beginning of both acquisition and analysis steps and were unchanged. Brightness and contrast were lightly adjusted after merging.

Chromatin Immunoprecipitation (ChIP)

ChIP was performed on cultured cells as previously described with slight modifications [117] Protein-DNA interactions were cross-linked in cells at 70% confluency with 1% paraformaldehyde (10 min, RT). Cross-linking was stopped by addition of 125 mM glycine for 10 min and the chromatin was sonicated to shear chromatin into fragments of 200–600 base pairs. The sheared chromatin was immunoprecipitated with 2 µg tri-methyl-histone H3 (Lys27) and di-methyl-histone H3 (Lys4), while negative control was incubated with mouse IgG and input DNA without antibody using the CHIP—IT Express HT Kit from Active Motif (Cat no: 53018) according to the manufacturer's instructions [Supplementary Table III]. A chromatin IP DNA Purification Kit (Cat No 58002 Active Motif) was used to purify the samples after CHIP before PCR was performed using Myh11 promoter primers [5' -CCC TCC CTT TGC TAA ACA CA - 3' and 5' - CCA GAT CCT GGG TCC TTA CA – 3] as previously published [117]. Sensimix SYBR® no-ROX Bioline Kit (QT650) was used to perform Real Time One-Step PCR according to the manufacturers' instructions. The antibodies used for ChIP are outlined in Supplemental Table I.

Quantitative PCR

Total RNA was prepared from cultured cells using the ReliaPrep™ RNA Cell Miniprep System kit from Promega according to the manufacturer's protocol. Two micrograms of RNA was used for reverse transcription with Rotor-Gene SYBR Green RT-PCR (QIAGEN) or The SensiMix™ SYBR® No-ROX (BioLine) protocols for Real TimeOne-Step RT-PCR using the Real Time Rotor-GeneRG-3000™ light cycler from Corbett Research using primers listed in Supplementary Table IV.

Western blot analysis

Total protein (~40µg) was resolved with SDS-PAGE and transferred to nitrocellulose membranes. The membrane was probed with primary antibodies [Supplementary Table II] and secondary anti-rabbit- anti-mouse antibody, HRP conjugated A5278 (Sigma) and anti-rabbit antibody, HRP conjugated A0545 (Sigma). Detection was performed using TMB T0565 (Sigma).

QUANTIFICATION AND STATISTICAL ANALYSIS

All data were determined from multiple individual biological samples and presented as mean values ± standard error of the mean (SEM). All *in vitro* experiments were performed in triplicate and repeated three times unless otherwise stated. All mice were randomly assigned to groups (including both male and female), and the analysis was performed blind by two groups. For statistical comparisons, all data was checked for normal gaussian distribution before parametric and non-parametric tests were performed. An unpaired two-sided Student's t-test was performed to compare differences between two groups and significance was accepted when $p \leq 0.05$. A one sample t Wilcoxon test was performed on fold changes and significance was accepted when $p \leq 0.05$. An ANOVA test was performed for multiple comparisons with a Sidak's multiple comparisons test for parametric data and a Dunn's Multiple comparison test for non-parametric data using GraphPad Prism software v8™. and significance was accepted when $p \leq 0.001$.

For PCA and LDA analysis, the cells were first classified to create a ground truth for each sample before the spectral data were normalized to one by dividing the fluorescence intensity at each wavelength by the average background intensity at that wavelength. Dimensionality reduction was achieved through a Multiclass Fisher's Linear Discriminant Analysis (Multiclass FLDA) preprocessing filter, as previously described using WEKA machine learning tool kit [118] and further analysed by LDA using the multivariate statistical package, PAST4 [53]. A scatter plot of specimens along the first two canonical axes produces maximal and second to maximal separation between all groups. The axes are linear combinations of the original variables as in PCA, and eigenvalues indicate amount of variation explained by these axes. When only two groups are analysed, a histogram is plotted. The data are classified by assigning each point to the group that gives minimal Mahalanobis distance to the group mean. The Mahalanobis

distance is calculated from the pooled within-group covariance matrix, giving a linear discriminant classifier. The given and estimated group assignments are listed for each point. In addition, group assignment is cross-validated by a leave-one-out cross-validation (jackknifing) procedure. To interrogate the photonic profiles from unknown 'mystery' groups, i.e. data that are not included in the discriminant analysis itself but are classified. In this way, it is possible to classify new datasets that are not part of the training set.

Supervised machine learning (ML). Supervised ML is a technique in which a model is trained on a range of inputs (or features) which are associated with a known outcome**.** Once the algorithm is successfully trained, it will be capable of making outcome predictions when applied to new data. Spectra from single cells across five broadband light wavelengths were first classified to create a ground truth for each sample before the data were normalized as before. Dimensionality reduction was achieved through Multiclass Fisher's Linear Discriminant Analysis (Multiclass FLDA), as previously described before MLP artificial neural network analysis was performed on the each dataset using the WEKA machine learning tool kit [52]. Once the dataset was loaded and pre-processed using the FLDA filter, it was processed using the "Classify" panel with the implementation for MLP artificial neural network (ANN) analysis. ANNs are algorithms which are loosely modelled on the neuronal structure observed in the mammalian cortex and are arranged with a number of input neurons, which represent the information taken from each of the features in the dataset which are then feed into any number of hidden layers before passing to an output layer in which the final decision is presented. The algorithm was iteratively improved using an optimization technique by changing the number of hidden layers (1,2.3., etc) and the momentum (0.1-0.5) and rate of learning (0.1-0.5) to reduce the error of prediction and then evaluated using cross-validation. The risk of over-fitting was mitigated against when our dataset was split into two segments; a training segment and a testing segment to ensure that the training model can generalize to predictions beyond the training sample. Each segment contained a randomly selected proportion of the features and their related outcomes which allowed the algorithm to associate certain features, or characteristics, with a specific outcome, and is known as training the algorithm. Once training was completed, the algorithm was then applied to the features in the testing dataset without their associated outcomes. The predictions made by the algorithm were then compared to the known outcomes of the testing dataset to establish

model performance. A total of 1008 cells were used to create this dataset across the five wavelengths. The model algorithm had 2 hidden layers and a momentum rate of 0.2 and a learning rate of 0.3. Performance was evaluated based on F1 scores, an aggregate of recall and precision, and on accuracy, the fraction of correct predictions.

EXPERIMENTAL MODEL AND SUBJECT DETAILS

Mice Breeding and Genotyping

All procedures were approved by the University of Rochester Animal Care Committee in accordance with the guidelines of the National Institutes of Health for the Care and Use of Laboratory Animals. S100β -EGFP/Cre/ERT2 transgenic mice (JAX Labs, stock #014160, strain name B6;DBA-Tg(S100β -EGFP/cre/ERT2)22Amc/j) express the eGFPCreER^{T2} (Enhanced Green Fluorescent Protein and tamoxifen inducible cre recombinase/ESR1) fusion gene under the direction of the mouse S100β promoter. Ai9 mice (Jax Labs, stock #007909, strain name B6.Cg-Gt(ROSA)26Sor$^{tm9(CAG\text{-}tdTomato)Hze}$ /J) express robust tdTomato fluorescence following Cre-mediated LoxP recombination. For lineage tracing experiments S100β-eGFP/Cre/ERT2–dTomato double transgenic mice of both genders were generated by crossing S100β -eGFP/Cre-ERT2 mice with Ai9 reporter mice. The tdTomato transgene expression pattern corresponds to genomically marked S100β and the eGFP transgene expression pattern corresponds to current expression of S100β. Genomic DNA for genotyping was prepared from mice tail and papered for genotyping by Proteinase K lysed, isopropanol precipitated and 70% ethanol washed. The number of animals used were approved based on the experiments effects size. All male and female mice were included in the study and were 8-10 weeks old.

Carotid Artery Ligation

Ligation of the left common carotid artery was performed essentially as described previously [78,84,119] 4 weeks after Tm-induced cre-recombination, in male and female S100β-eGFP/Cre/ERT2–dTomato double transgenic mice. Prior to surgery mice received a single dose of Buprenorphine SR (sustained release) analgesia (0.5-1.0 mg/kg SQ) (and every 72 hrs thereafter as needed). The animal was clipped and the surgical site prepped using betadine solution and alcohol. A midline cervical incision was made. For partial carotid artery ligation, with the aid of a dissecting microscope, the left external and internal carotid arterial branches were isolated and ligated with 6-0 silk suture reducing left carotid blood flow to flow via the patent occipital artery. The neck incision (2 layers, muscle and skin) was sutured closed. Partial ligation of the left carotid artery in this manner resulted in a decrease (~80%) in blood flow, leaving an intact endothelial monolayer. Buprenorphine was administered at least once post-op 6-12 hrs. For complete ligation, the left common carotid was isolated and ligated just

beneath the bifurcation with 6-0 silk suture. In sham surgery group, carotid was similarly manipulated but not ligated. The neck incision (2 layers, muscle and skin) was sutured closed and the animal allowed recover under observation. After 3, 7, 14 and 21 days, mice were perfused with 4% PFA via the left ventricle for 10 min, and carotid arteries were harvested after 14 and 21 d for analysis.

Cell culture and harvesting

Murine aortic SMCs (Movas (ATCC® CRL-2797™) were cultured in Dulbeco's Modified Eagles growth medium (DMEM) supplemented with 10% Fetal Bovine Serum, 2 mM L-glutamine) and 1% penicillin-streptomycin. Murine embryonic C3H/10T1/2 cells (ATCC® CRL-226™) were grown in Eagle's Basal medium supplemented with heat-inactivated fetal bovine serum to a final concentration of 10% and 2mM L-glutamine and 1% penicillin-streptomycin. Murine vSCs from mouse aorta were grown in maintenance media (MM) containing DMEM media supplemented with chick embryo extract (2%), FBS embryonic qualified (1%, ATCC), B-27 Supplement, N-2 Supplement (Cell Therapy Systems), recombinant mouse bFGF (0.02 µg/mL), 2-Mercaptoethanol (50 nM), retinoic acid (100 nM), Penicillin-Streptomycin (1%). J774A.1 mouse BALB/c monocyte macrophages were a kind gift from Prof Christine Loscher, DCU and were grown in DMEM supplemented with 10% Fetal Bovine Serum, 2 mM L-glutamine and 1% Penicillin-Streptomycin. Human Burkitt's lymphoma B cells (Ramos B cells) were a kind gift from Prof Dermot Walls, DCU and were grown in RPMI 1640 supplemented with 10% Fetal Bovine Serum (Heat inactivated), and 1% penicillin-streptomycin.

Isolation of S100β/Sca1^{+} murine resident vascular stem cells (vSCs)

Using an optimised enzymatic cell dissociation technique protocol, mVSc from murine aorta were isolated using sequential seeding on adherent and non—adherent plates. Mouse thoracic aortas (4 at a time) were harvested and placed in cold Hank's solution for adipose tissue removal and lumen rinsing. The adventitia was enzymatically removed by incubation of the vessels in collagenase solution [i.e., MEMα nucleosides GlutaMAX™ (2 mL) containing Collagenase type 1A (0.7 mg/mL), soybean trypsin inhibitor (50 mg/mL), and bovine serum

albumin (1 mg/mL)] for approx. 10-20 min at 37°C. Once the adventitia became lose, it was carefully removed as an intact layer using forceps under a dissecting microscope. The aorta was divided into aortic arch (AA) and thoracic aorta (TA) regions and cut into 1 mm pieces and digested with Elastase type III (Sigma) at 37°C. Dispersed cells were centrifuged and washed twice in warm maintenance medium (MM) (DMEM supplemented with 2% chick embryo extract, 1% FBS, 0.02 µg/mL, bFGF basic protein, B-27 Supplement, N-2 supplement, 1% Penicillin-Streptomycin, 50 nM 2-Mercaptoethanol and 100 nM retinoic acid) before seeding (1st seeding) on a 6-well non-adherent plate in MM. At 48 h, suspension cells were transferred (2nd seeding) to a fresh well of a CELLstart™ pre-coated 6-well plate in MM. MM was added to the remaining cells in the non-adherent surface. Cells were incubated at 37°C, 5% CO_2 for 1 week with minimal disturbance. The stem cells exhibited a uniform neural-like morphology in low density culture adopting a dendritic-like tree shape and retaining their morphological characteristics at low density throughout repeated passage. Cells were fed with MM every 2-3 days and passaged every 3-4 days or when ~70% confluent.

Acknowledgments:

A. We thank Diana Scott for histological tissue processing, and Drs Linda Callahan and Paivi Jordan (University of Rochester, NY) for confocal microscope expertise and Dr Tim Downing (Dublin City University) for the advice on the computational and statistical analysis. We thank Prof Robert Forster and Dr Phil Cummins for critically reviewing the manuscript and for their insights and helpful discussions.

B. This research was funded in part by Science Foundation Ireland grant SFI-11/PI/1128, Health Research Board (HRB) of Ireland grant HRA-POR-2015-1315, and the European Union's INTERREG VA Programme, managed by the Special EU Programmes Body (SEUPB) to PAC, and NIH R21AA023213 and RO1AA024082 to EMR, Irish Research Council (IRC) GOIPG/2014/43 (M.DiL), Fraunhofer-Gesellschaft under the SFI Strategic Partnership Programme [Grant Number 16/SPP/3321] Science Foundation Ireland [Grant Number: 10/CE/B1821]; the ERDF; the LiPhos project funded by the European Commission [Grant Number: 317916] to JD.

C. The authors declare no competing financial interests.

D. E.M.R, D.M., and W.L., performed the animal experiments and M.DiL performed the blind analysis of the confocal images. C.M., M.DiL., R.H., D.B., E.F., performed the murine cell culture experiments, D.B., MDiL and R.H., performed the ChIP analysis. D.K., A.L., L.J., and J.D. developed the LoaD platform and C.M, A.O., D.K, D.C., K.H., and R.H performed the single cell photonic analysis studies. E.F and P.A.C performed the PCA/LDA and WEKA analysis. E.M.R., C.M., and P.A.C drafted the manuscript, revised the manuscript and discussed the results. E.M.R., D.K., CM and P.A.C., designed and coordinated the experiments, interpreted the data, revised and confirmed the paper. All authors reviewed and confirmed the manuscript.

E. Correspondence to Paul A. Cahill (paul.cahill@dcu.ie)

F. Several datasets were generated and analysed during the current study.

Supplementary Table I

Antibodies and their corresponding dilutions used in immunohistochemistry.

Antibody/Product Name	Supplier/Product Number	Dilutions
Rabbit anti-mouse/rat alpha smooth muscle cell α-actin antibody	Abcam (ab5694)	1/200
Anti-Actin, α-Smooth Muscle antibody, Mouse monoclonal	Sigma (A5228)	1/200
Anti-S100-β (CT) Antibody, clone EP1576Y, rabbit monoclonal	Millipore (04-1054)	1/100
Chicken anti-GFP antibody	Abcam (ab13970)	1/1000
Rabbit Anti-RFP/dT antibody	Abcam (ab62341)	1/1000

Supplementary Table II

Antibodies and their corresponding dilutions used in immunocytochemistry/western blot.

Antibody/Product Name	Supplier/Product Number	Dilutions
Rabbit anti-mouse Calponin [EP798Y]	Abcam (ab46794)	1/200
Goat anti-mouse/rat/human smooth muscle Myosin heavy chain	Santa Cruz (sc-79079)	1/200
Rabbit Anti-S100β	Merck Millipore (ABN59)	1/100
Rabbit Anti-mouse/rat S100β [EP1576Y]	Abcam (ab52642)	1/100
Alexa Fluor® 488 Goat anti-mouse IgG	Invitrogen (A-11001)	1/1000

Alexa Fluor® 488 Goat anti-rabbit IgG	Invitrogen (A-11008)	1/1000
Alexa Fluor® 488 Donkey anti-goat IgG	Invitrogen (A-11055)	1/1000

Supplementary Table III

Antibodies used in Chromatin Immunoprecipitation (ChIP)

Antibody/Product Name	Supplier/Product Number
Rabbit anti-mouse Tri-Methyl-Histone H3 (Lys27) [C36B11]	Cell Signalling Technology (9733S)
Rabbit anti-mouse Di-Methyl-Histone H3 (Lys4) [C64G9]	Cell Signalling Technology (9725S)
Normal Rabbit IgG (ChIP graded)	Cell Signalling Technology (2729)

Supplementary Table IV

Customised primers used in this study from Integrity DNA Technology (IDT).

Customised primer		Sequences
Mm_Sm-mhc (Myh11)	Forward	5' - GCA GTG AGC TCT CAG TCA TC - 3’
	Reverse	5' - CAA TGC CTC CTC TGA CAA GT - 3'
Mm_Cnn1	Forward	5’ - GCT TGT CTG CTG AAG TAA AGA AC - 3'
	Reverse	5’ - TCC ATG AAG TTG TTC CCG ATG - 3'
Mm_Hprt	Forward	5’ - GGC TAT AAG TTC TTT GCT GAC CTG C - 3'
	Reverse	5’ - GCT TGC AAC CTT AAC CAT TTT GGG - 3'
Mm_Gaphd	Forward	5’ - GCC TCC AAG GAG TAA GAA AC - 3'

	Reverse	5’ - GCC TCC AAG GAG TAA GAA AC - 3'
Mm_ Sm-mhc (Myh11)	Forward	5’ - CCC TCC CTT TGC TAA ACA CA - 3'
for ChIP PCR	Reverse	5’ - CCA GAT CCT GGG TCC TTA CA - 3'

Primers used in this study from QIAGEN.

Primer	Product Name	Product Code
mHprt-1	Mm_Hprt_1_SG QuantiTect Primer Assay	QT00166768
mGapdh	Mm_Gapdh_3_SG QuantiTect Primer Assay	QT01658692

Figure Legends

Figure 1. **Single cell photonics from normal and injured vessels *ex vivo* following flow restriction. A.** Representative haematoxylin and eosin (H&E) staining of LCA from sham and ligated vessels 14 days post-ligation (A: Adventitia, M: Media, I:Intima and NI:Neointima). **B.** Morphometric analysis of adventitial, medial and intimal volumes within the LCA in sham and ligated arteries; (#p≤0.05, n=3). **C.** Representative immunohistochemical analysis of Myh11 (red) and α-actin expression (red) and DAPI nuclei staining (blue) in adventitial, medial and intimal layers of the LCA from sham and ligated carotid arteries. **D.** Representative immunoblot of Myh11 expression in the LCA from sham and ligated carotid artery (n=3). **E.** Schematic of capture of individual cells using the LoaD platform. **F.** Representative image of formalin-fixed cells from sham and ligated vessels captured on a V-cup using the LoaD platform. **G.** Single cell auto-fluorescence photon emissions across five broadband light wavelengths (λ465, λ530, λ565, λ630 and λ670 nm with a bandwidth of 20 nm) of cells isolated from sham and ligated LCA *ex vivo*. Data are the mean ± SEM of 178 cells/group of Log10 photons from 178 cells/group from 6 pooled vessels, #p≤0.001 vs sham. **H**. Log2 fold increase over background of single cell auto-fluorescence photon emissions of cells isolated from sham and ligated LCA across five wavelengths. Data are the mean ± SEM of 178 cells/group from 6 pooled vessels, #p≤0.001 vs sham. **I.** PCA biplots of single cell photon analysis from sham (black) and ligated (orange) vessels. Each λ variable in the PCA biplot has an associated arrow pointing in the direction of increasing values of that λ variable and is representative of the eigenvectors (loadings). **J.** PCA loading plots of single cell photon analysis from sham (black) and ligated (orange) cells *ex vivo* compared to Ramos B cells *in vitro* (red). Data are from 411 cells across the five wavelengths. **K.** LDA plots of single cell photons from sham (black) and ligated (orange) vessels **L.** Confusion matrix of cells assigned to each group by the classifier. True class represents the given group assignment and predicted class represents the estimated group assignment following a leave-one-out cross-validation procedure.

Figure 2. Single cell photonics of B-cells and J774A.1 macrophages *in vitro*. A-D. Single cell auto-fluorescence photon emissions across five wavelengths from (A, C) Ramos B cells and (B, D) J774A.1 cells *in vitro* compared to sham (A, B) and ligated cells (C,D) *ex vivo*. Data are the

Log2 fold increase and represent the mean ± SEM of 55-178 cells/group, #p≤0.001 vs Sham (A,B) Ligated (C,D). **E.** PCA loading plots of sham (black), ligated (orange), Ramos B (red) and J774A.1 (blue) cells. **F.** LDA plots of sham (black), ligated (orange) cells *ex vivo* and Ramos B (red) and J774A.1 (blue) cells *in vitro.* Data are from 466 cells across the five wavelengths **G.** Confusion matrix of true class and predicted class following a leave-one-out cross-validation procedure by the LDA classifier.

Figure 3. **Single cell photonics of aortic SMCs ex vivo and cultures aortic Movas SMCs *in vitro*. A.** Single cell auto-fluorescence photon emissions across five wavelengths from freshly isolated aortic SMCs and cultured aortic Movas SMCs *in vitro.* Data are the Log2 fold increase and represent the mean ± SEM of 55 cells/group, #p≤0.001. **B.** Single cell auto-fluorescence photon emissions of aortic and Movas SMCs compared to Ramos B cells. Data are the Log2 fold increase and represent the mean ± SEM of 55 cells/group, #p≤0.001. **C.** LDA plots of aortic SMC (blue), Movas SMC (red) and Ramos B (black) cells *in vitro*. Data are from 165 cells across the five wavelengths **D-G.** Single cell auto-fluorescence photon emissions from (D,F) aortic SMC and (E, G) Movas SMC cells *in vitro* compared to sham (D, E) and ligated cells (F, G) *ex vivo*. Data are the Log2 fold increase and represent the mean ± SEM of 55-178 cells/group, #p≤0.001 vs Sham (D,E) Ligated (F,G). **H.** LDA plots of sham (black), ligated (orange) cells *ex vivo* compared to aortic SMCs (blue) and Movas SMC (Red) cells *in vitro* **G.** Confusion matrix of true class and predicted class following a leave-one-out cross-validation procedure by the LDA classifier. Data are from 466 cells across five wavelengths.

Figure 4. Single cell photonics of murine bone marrow-derived mesenchymal stem cells (mMSCs) before and after myogenic differentiation *in vitro.* A. Representative immunocytochemical analysis of Cnn1 (green), Myh11 (green) and DAPI nuclei staining (blue) in mMSCs before and after treatment of cells with media supplemented with TGF-β1 (2ng/mL). **B.** The fraction of $Cnn1^+$ and $Myh11^+$ cells before and after treatment of cells with media supplemented with TGF-β1 (2ng/mL). Data are the mean ± SEM of 5 wells, #p<0.05 vs control. **C.** Fold enrichment of the stable SMC histone modification, H3K4me2 and repressive histone modification, H3K27me3 at the Myh11 promoter in fresh mouse aorta, cultured Movas SMCs and undifferentiated mMSCs in the absence or presence of TGF-β1 (2ng/mL) for 7d. Data are mean ± SEM of a representative experiment performed in triplicate, #p<0.05 vs

control (-) TGF-β1 levels. **D.** Log2 fold change in Cnn1 mRNA levels in mMSCs and representative immunoblot of Cnn1 and Myh11 protein expression in lysates in response to TGF-β1 (2ng/mL). Data are mean ± SEM of n=5, #p≤0.05 considered as significant. **E-G.** Single cell auto-fluorescence photon emissions from MSCs in the absence or presence of TGF-β1 (2ng/mL) for (E) 7 (F) 14 and (G) 28 d *in vitro.* Data are the Log2 fold increase and represent the mean ± SEM of 55-79 cells/group, #p≤0.001. **H.** LDA plots of MSC (cyan) before and after treatment with TGF-β1 (2ng/mL) for 7d (brown), 14d (magenta) and 28d (purple) cells *in vitro*. Data are the Log2 fold increase and represent the mean ± SEM of 55-79 cells/group, #p<0.001. **I-K.** Single cell auto-fluorescence photon emissions from MSCs in the absence or presence of TGF-β1 (2ng/mL) 28 d *in vitro* compared to (I, J) sham and (K) ligated cells *ex vivo*. Data are the Log2 fold increase and represent the mean ± SEM of 55-178 cells/group, #p≤0.001 vs Sham (I,J) Ligated (K). **L.** PCA loading plots of sham (black), ligated (orange) and MSC (cyan) before and after myogenic differentiation with TGF-β1 for 7d (brown), 14d (magenta) and 28d (purple). **M.** LDA plots of sham (black), ligated (orange) and MSC (cyan) before and after treatment with TGF-β1 (2ng/mL) for 7d (brown), 14d (magenta) and 28d (purple) cells. Data are from 624 cells across 5 wavelengths. **N.** Single cell auto-fluorescence photon emissions from Ramos B cells in the absence or presence of TGF-β1 (2ng/mL) 14d. Data are the Log2 fold increase and represent the mean ± SEM of 55 cells/group, #p<0.001. **O.** Confusion matrix of true class and predicted class following a leave-one-out cross-validation procedure by the LDA classifier. Data are from 624 cells across 5 wavelengths.

Figure 5. Single cell photonics of C3H/10T1/2 mesenchymal stem cells before and after myogenic differentiation *in vitro.* A. Representative immunocytochemical analysis of Cnn1 (green), Myh11 (green) and DAPI nuclei staining (blue) in C3H/10T1/2 cells before and after treatment of cells with media supplemented with TGF-β1 (2ng/mL) for 7d. **B.** The fraction of $Cnn1^+$ and $Myh11^+$ cells before and after treatment of cells with media supplemented with TGF-β1 (2ng/mL). Data are the mean ± SEM of 5 wells, #p≤0.05 vs control. **C.** Representative immunoblot of Cnn1 and Myh11 protein expression in C3H/10T1/2 lysates in response to TGF-β1 (2ng/mL). **D.** Log2 fold change in Cnn1 mRNA levels in C3H/10T1/2 cells in response to TGF-β1 (2ng/mL). Data are the mean ± SEM n=5, #p≤0.05. **E.** Single cell auto-fluorescence photon emissions from C3H/10T1/2 in the absence or presence of TGF-β1 (2ng/mL) 7 d *in vitro*. Data are the Log2 fold increase and represent the mean ± SEM of 55 cells/group,

#p≤0.001 vs control. **F.** PCA loading plots of C3H/10T1/2 cells before (blue) and after myogenic differentiation with TGF-β1 for 7d (yellow). Data are 55 cells/group. **G-H.** PCA loading plots and LDA of C3H/10T1/2 cells before (blue) and after myogenic differentiation with TGF-β1 for 7d (yellow) compared to Ramos B cells (red) and J774A.1 macrophages (black). Data are 55 cells/group. **I-J.** Single cell auto-fluorescence photon emissions from C3H/10T1/2 in the absence or presence of TGF-β1 (2ng/mL) 7 d *in vitro* compared to sham (I) and ligated cells (J) *ex vivo.* Data are the Log2 fold increase and represent the mean ± SEM of 55-178 cells/group, #p<0.001. **K.** PCA loading plots of sham (black), ligated (orange) and C3H/10T1/2 cells before (blue) and after treatment with TGF-β1 (2ng/mL) for 7d (yellow). **L.** LDA plots of sham (black), ligated (orange) cells *ex vivo* and C3H/10T1/2 cells before (blue) and after treatment with TGF-β1 (2ng/mL) for 7d (yellow*) in vitro.* **M.** Confusion matrix of true class and predicted class following a leave-one-out cross-validation procedure using the LDA classifier. Data are from 466 cells across five wavelengths.

Figure 6. Lineage tracing analysis of marked perivascular S100β cells following flow restriction. A. Schematic diagram showing genetic lineage tracing using S100β-CreERT2-Rosa26-tdTomato. **B.** Schematic diagram showing protocol for Tm injections before ligation after 4 week Tm washout. **C.** Morphometric analysis of adventitial, medial, intimal and luminal volumes in male and female S100β-CreERT2-Rosa26-tdTomato mice following complete ligation of the left carotid artery (LCA) for 21 d. Data are from 4 animals per experimental group. **D.** Representative confocal fluorescence images of DAPI nuclei (blue) and S100β-tdT+ (red) cells in sham and ligated LCA in corn oil (control) treated animals. Representative images shown; 4 animals per experimental group. Scale bar = 50µm. **E.** Representative confocal fluorescence images of DAPI nuclei (blue), S100β-tdT$^+$ (red) cells S100β-eGFP$^+$ cells in sham and ligated LCA in tamoxifen (Tm) treated animals. Representative images are from 4 animals per experimental group. Scale bar = 50µm. **F.** Cumulative analysis of the number of DAPI nuclei/hpf in the adventitial, medial and intimal layers from the contralateral RCA and ligated LCA. Data are the mean ± SEM of 10-20 images/group, #p≤0.05. **G.** Cumulative analysis of the fraction of S100β-eGFP$^+$ cells within the adventitia (A), media (M), and neointima (NI) of RCA and ligated LCA. Data are the mean ± SEM of 15-20 sections per experimental group, #p≤ 0.05 from 4 animals per group. **H.** Cumulative analysis of the fraction of S100β-tdT$^+$ cells within the

adventitia (A), media (M), and neointima (NI) of RCA and ligated LCA. Data are the mean ± SEM of 15-20 sections per experimental group, #p≤ 0.05 from 4 animals per group.

Figure 7. Single cell photonics of S100β$^+$ vascular stem cells (mVSc) before and after myogenic differentiation *in vitro.* **A.** Representative immunocytochemical analysis of Cnn1 (green) and DAPI nuclei staining (blue) in mVSc before and after treatment of cells with media supplemented with TGF-β1 (2ng/mL), Jag1 (1µg/mL) and SHh (0.5µg/mL) for 14d. **B.** The fraction of Cnn1$^+$ cells before and after treatment of cells with media supplemented with TGF-β1 (2ng/mL), Jag1 (1µg/mL) and SHh (0.5µg/mL) for 14d. Data are the mean ± SEM of 3 experiments, #p≤0.05 vs control. **C.** Log2 fold change in Cnn1 mRNA levels before and after treatment of cells with media supplemented with TGF-β1 (2ng/mL), Jag1 (1µg/mL) and SHh (0.5µg/mL) for 7d. Data are the mean ± SEM n=3, #p≤0.05 vs control. **D.** Fold enrichment of the stable SMC histone modification, H3K4me2 and repressive histone modification, H3K27me3 at the Myh11 promoter in fresh mouse aorta (Aorta), mouse embryonic stem cells (ESC), and undifferentiated S100β$^+$ mVSc before (mVSc) and after treatment of cells with media supplemented with TGF-β1 (2ng/mL), Jag1 (1µg/mL) and SHh (0.5µg/mL) for 7 d. Data are representative of n=3, #p<0.05 vs control. **E-G.** Single cell auto-fluorescence photon emissions from mVSc in the absence or presence TGF-β1 (2ng/mL), Jag1 (1µg/mL) and SHh (0.5µg/mL) for 14 d *in vitro*. Data are the Log2 fold increase and represent the mean ± SEM of 55 cells/group, #p≤0.001 vs control. **H-J.** Individual PCA loading plots of mVSc before (blue) and after myogenic differentiation with (H) TGF-β1 (green), (I) Jag1 (yellow) and (J) SHh (red). **K-M.** Individual LDA plots of mVSc before and after myogenic differentiation with (K) TGF-β1, (L) Jag1 and (M) SHh. **N.** Cumulative PCA loading plots of mVSc before (blue) and after myogenic differentiation with (H) TGF-β1 (green), (I) Jag1 (yellow) and (J) SHh (red). **O.** Cumulative LDA plots of mVSc before and after myogenic differentiation with (K) TGF-β1, (L) Jag1 and (M) SHh. **P.** Confusion matrix of true class and predicted class following a leave-one-out cross-validation procedure by the LDA classifier. Data are from 219 cells across five wavelengths.

Figure 8. Single cell photonics identifies S100β resident vascular stem cells and their myogenic progeny within ligated vessels. A-C. Single cell auto-fluorescence photon emissions from Sham cells *ex vivo* compared to mVSc in the presence (A) TGF-β1 (2ng/mL),

(B) Jag1 (1µg/mL) and (C) SHh (0.5µg/mL) for 14 d *in vitro*. Data are the Log2 fold increase and represent the mean ± SEM of 55-178 cells/group, #p≤0.001 vs control. **D-F.** Single cell auto-fluorescence photon emissions from ligated cells *ex vivo* compared to mVSc in the presence (D) TGF-β1 (2ng/mL), (E) Jag1 (1µg/mL) and (F) SHh (0.5µg/mL) for 14 d *in vitro*. Data are the Log2 fold increase and represent the mean ± SEM of 55-178 cells/group, #p≤0.001 vs control. **G.** Cumulative PCA loading plots of sham (black), ligated (orange) and mVSc before (blue) and after myogenic differentiation with (H) TGF-β1 (green), (I) Jag1 (yellow) and (J) SHh (red). **H.** Cumulative LDA plots of sham (black), ligated (orange) and mVSc before and after myogenic differentiation with TGF-β1 (green), Jag1 (yellow) and SHh (red). **I.** Confusion matrix of true class and predicted class following a leave-one-out cross-validation procedure by the LDA classifier. Data are from 575 cells across five wavelengths. **J-K.** Percentage of cells in sham and ligated vessels predicted as mVSc and their myogenic progeny by LDA classifier. Data are from 575 cells across five wavelengths **L-M.** Percentage of cells in sham and ligated vessels classified as aortic SMCs, Movas SMCs and mVSc and their myogenic progeny when trained with datasets by LDA classifier. Data are from 356 cells. **N-O.** Percentage of cells in sham and ligated vessels classified as sham cells, aortic SMCs, Movas SMCs and mVSc and their myogenic progeny when trained with datasets by the LDA classifier. Data are from 356 cells across five wavelengths. **P.** Graphic representation of percentage of cells in sham and ligated vessels when trained with sham cells, aortic SMCs, Movas SMCs and mVSc and their myogenic progeny by LDA classifier.

Figure 9. Single cell photonics of all cells identifies S100β resident vascular stem cells and their myogenic progeny within ligated vessels using an LDA classifier. A. Confusion matrix of true class and predicted class of all cells following a leave-one-out cross-validation procedure by the LDA classifier. The LDA algorithm was trained using single cell photonic analysis from (i) sham cells, (ii) aortic SMCs, (iii) Movas SMCs, (iv) J774A.1 macrophages, (v) Ramos B cells, (vi) MSCs and their myogenic progeny, (vii) S100β mVSc and their myogenic progeny. Data are from 885 cells **B.** Percentage of cells in sham vessels using the LDA classifier when trained with all cells. Data are from 178 cells. **C.** Percentage of cells in ligated vessels using the LDA classifier when trained with all cells. Data are from 178 cells **D.** Graphic representation of percentage of cells in sham and ligated vessels when trained with all cell using the LDA classifier.

Figure 10. Supervised machine learning identifies S100β$^+$ mVSc-derived myogenic progeny within ligated vessels. A. Graphic representation of the MLP neural network algorithm. **B.** Confusion matrix of true class and predicted class of following training with (i) sham cells, (ii) ligated cells (iii) aortic SMCs, (iv) Movas SMCs, (v) J774A.1 macrophages, (vi) MSCs and their myogenic progeny and (vii) S100β mVSc and their myogenic progeny using MLP neural network analysis. **C.** Percentage of cells in sham vessels classified using MLP neural network analysis on trained dataset. The dataset consisted of 1008 cells across five wavelengths. **D.** Percentage of cells in ligated vessels classified using the MLP neural network analysis on trained dataset. The dataset consisted of 178 cells across five wavelengths **E.** Graphic representation of percentage of cells in sham and ligated vessels using MLP neural network analysis.

Figure 11. **Elastin and Coll 3A1 contribute to the photonic intensity of stem cell-derived myogenic progeny at λ565 ± 20 nm wavelength. A.** PCA biplots of single cell photon analysis from MSC, mVSc and C3H/10T1/2 cells in the absence or presence of TGF-β1. Each λ variable in the PCA biplot has an associated arrow pointing in the direction of increasing values of that λ variable and is representative of the eigenvectors (loadings). The λ565 variable strongly influences PC1 when cells undergo myogenic differentiation. **B.** Log2 fold changes in single cell auto-fluorescence photon emissions at λ565 nm in sham and ligated cells *ex vivo*, MSC and mVSc following myogenic differentiation. Data are the mean ± SEM of 55-178 cells/group, #p≤0.01. **C.** Log2 fold changes in mRNA levels for elastin and Coll3A1 in MSCs following treatment with TGF-β1 for 7 d. Data are the mean ± SEM of n= 3, #p≤0.05 vs control. **D.** Log2 fold changes in mRNA levels for elastin and Coll 3A1 in mVSc following treatment with TGF-β1 for 7 d. Data are the mean ± SEM of n= 3, #p≤0.05 vs control **E.** Log2 fold changes in mRNA levels for elastin and Coll 3A1 in mVSc following treatment with Jag1 for 7 d. Data are the mean ± SEM of n= 3, #p≤0.05 vs Fc control. **F.** Log2 fold changes in mRNA levels for elastin and Coll3A1 in response to TGF-β1 (2ng/mL) following siRNA knockdown of elastin and Coll3A1, respectively. Data are the mean ± SEM of n= 3, #p≤0.05 vs scrambled control. **G.** Log2 fold changes in single cell auto-fluorescence photon emissions at λ565 nm in response to TGF-β1 (2ng/mL) following siRNA knockdown of elastin and Coll3A1, respectively. Data are the mean ± SEM of n= 3, #p≤0.05 vs scrambled control.

The contribution of elastin and Coll 3A1 to the enhanced AF profile of stem-cell derived myogenic progeny at λ565 ± 20nm wavelength. (a) Fold change in elastin and Coll 3A1 mRNA levels in MSC following treatment of cells with TGF-β1 (10ng/mL) for 48h; Data are the mean ± SEM of two independent experiments performed in triplicate. *$p<0.05$ vs control (without TGF-β1); (b) Percent elastin and Coll 3A1 mRNA levels in MSC following elastin and Coll 3A1 knockdown with specific siRNA duplexes after 72 h; (insert) Transfection efficiency of siRNA duplexes using tagged TyesiRNA; (c) Single cell AF intensity analysis of individual MSCs on a V-cup using the LoaD platform following transfection of cells with siRNA duplexes targeted against elastin and Coll 3A1 after 72 h. Data are the mean ± SEM of 55 cells/group from 2 independent experiments, *$p<0.05$ vs scrambled control; (d) Single cell AF intensity analysis of individual MSCs on a V-cup using the LoaD platform following elastin and Coll 3A1 depletion in the absence or presence of TGF-β1 (10ng/mL) for 7 d; Data are the mean ± SEM of 55 cells/group from 3 independent experiments, *$p<0.05$ vs scrambled control, #$p<0.05$ vs TGF-β1 treated cells.

Figure 1

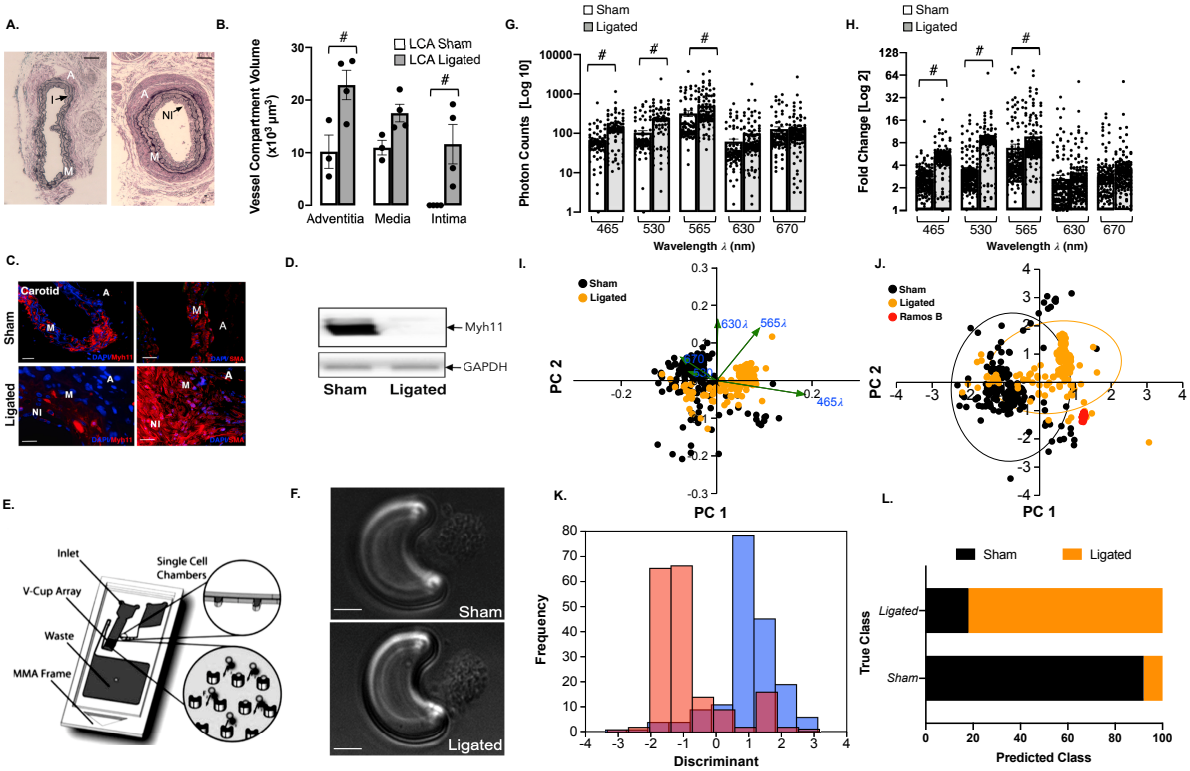
A.
B.
LCA Sham
LCA Ligated
Vessel Compartment Volume (x10^3 µm^3)
Adventitia
Media
Intima
G.
Sham
Ligated
Photon Counts [Log 10]
Wavelength λ (nm)
H.
Fold Change [Log 2]
C.
Carotid
Sham
Ligated
D.
Myh11
GAPDH
Sham
Ligated
I.
PC 1
PC 2
J.
Ramos B
E.
Inlet
Single Cell Chambers
V-Cup Array
Waste
MMA Frame
F.
Sham
Ligated
K.
Frequency
Discriminant
L.
True Class
Predicted Class

Figure 2

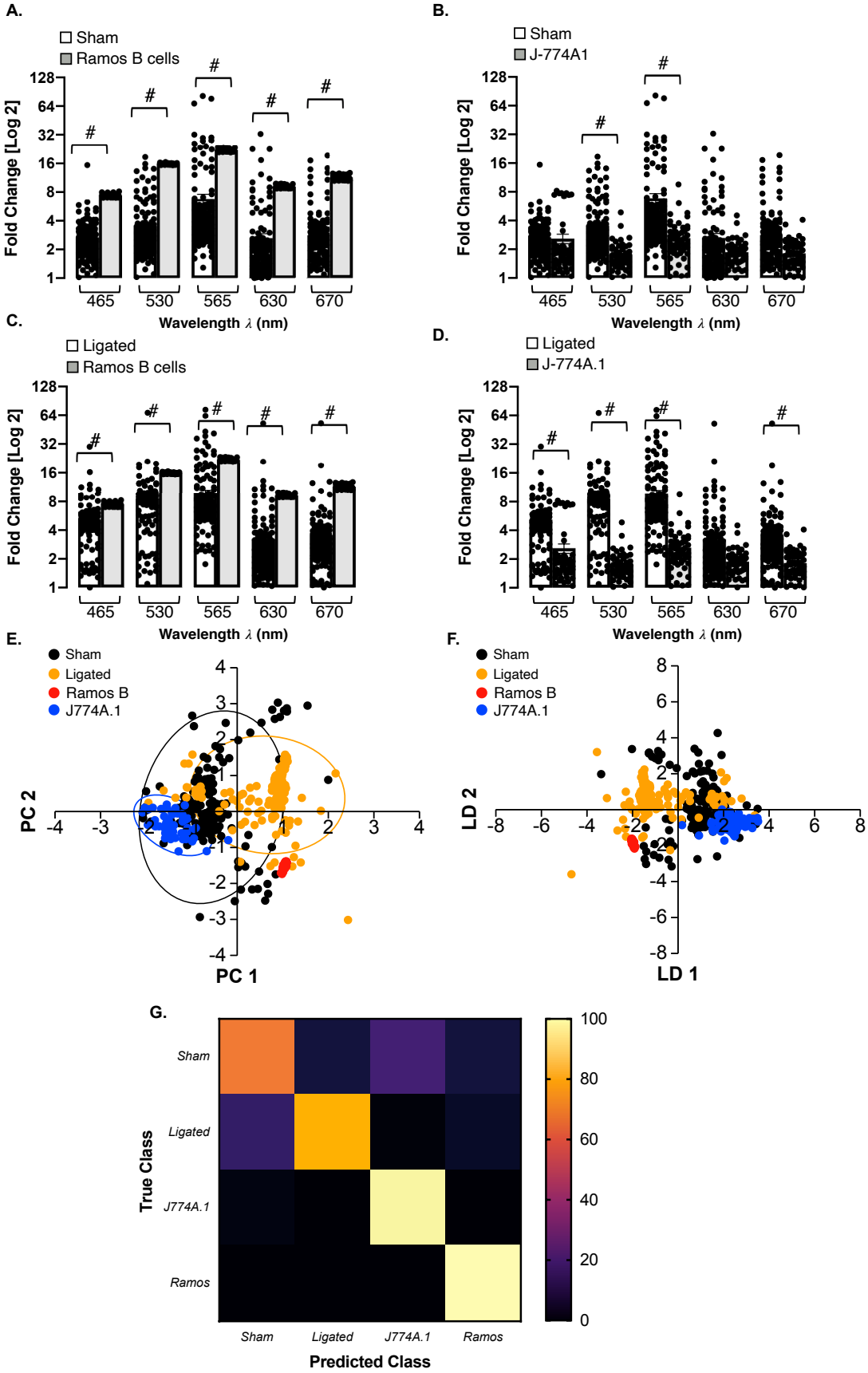
A.
Sham
Ramos B cells
Fold Change [Log 2]
Wavelength λ (nm)
B.
Sham
J-774A1
C.
Ligated
Ramos B cells
D.
Ligated
J-774A.1
E.
Sham
Ligated
Ramos B
J774A.1
PC 1
PC 2
F.
LD 1
LD 2
G.
True Class
Predicted Class
Sham
Ligated
J774A.1
Ramos

Figure 3

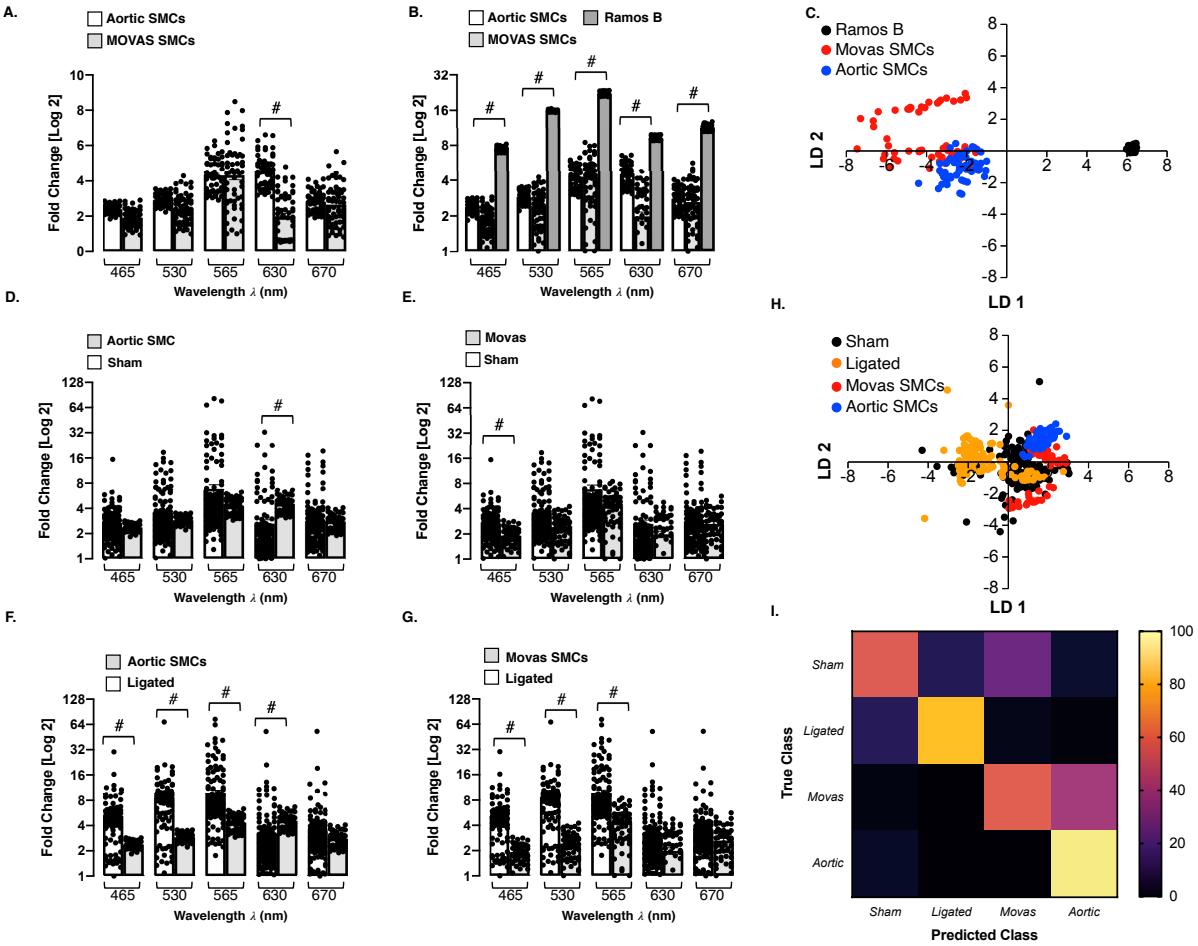
A.
Aortic SMCs
MOVAS SMCs
Fold Change [Log 2]
Wavelength λ (nm)
B.
Aortic SMCs
Ramos B
MOVAS SMCs
C.
Ramos B
Movas SMCs
Aortic SMCs
LD 2
LD 1
D.
Aortic SMC
Sham
E.
Movas
Sham
H.
Sham
Ligated
Movas SMCs
Aortic SMCs
F.
Aortic SMCs
Ligated
G.
Movas SMCs
Ligated
I.
True Class
Predicted Class
Sham
Ligated
Movas
Aortic

Figure 4

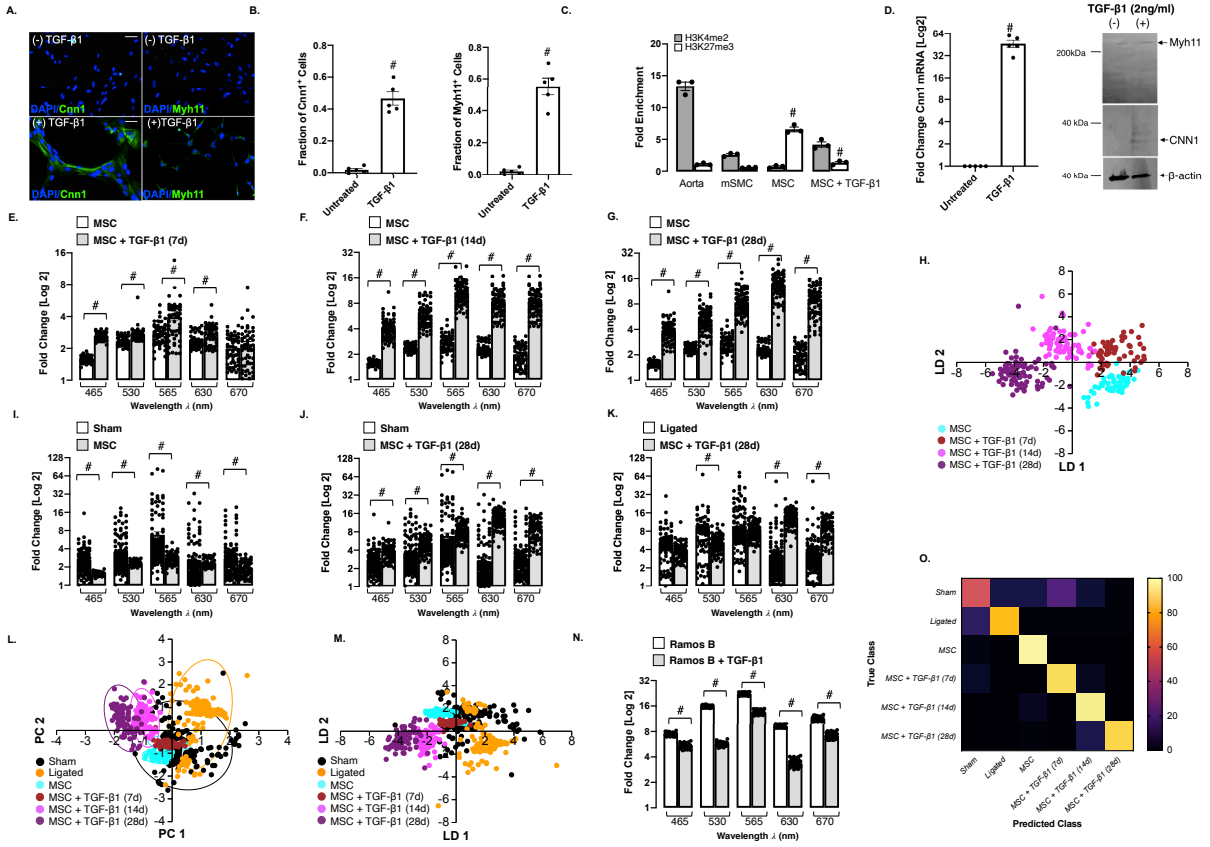
A.
(-) TGF-β1
(-) TGF-β1
DAPI/Cnn1
DAPI/Myh11
(+) TGF-β1
(+)TGF-β1
DAPI/Cnn1
DAPI/Myh11
B.
Fraction of Cnn1+ Cells
Fraction of Myh11+ Cells
Untreated
TGF-β1
C.
H3K4me2
H3K27me3
Fold Enrichment
Aorta
mSMC
MSC
MSC + TGF-β1
D.
Fold Change Cnn1 mRNA [Log2]
Untreated
TGF-β1
TGF-β1 (2ng/ml)
(-)
(+)
200kDa
40 kDa
40 kDa
Myh11
CNN1
β-actin
E.
MSC
MSC + TGF-β1 (7d)
Fold Change [Log 2]
Wavelength λ (nm)
F.
MSC
MSC + TGF-β1 (14d)
G.
MSC
MSC + TGF-β1 (28d)
H.
LD 2
LD 1
MSC
MSC + TGF-β1 (7d)
MSC + TGF-β1 (14d)
MSC + TGF-β1 (28d)
I.
Sham
MSC
J.
Sham
MSC + TGF-β1 (28d)
K.
Ligated
MSC + TGF-β1 (28d)
L.
PC 2
PC 1
Sham
Ligated
MSC
MSC + TGF-β1 (7d)
MSC + TGF-β1 (14d)
MSC + TGF-β1 (28d)
M.
LD 2
LD 1
N.
Ramos B
Ramos B + TGF-β1
O.
True Class
Predicted Class
Sham
Ligated
MSC
MSC + TGF-β1 (7d)
MSC + TGF-β1 (14d)
MSC + TGF-β1 (28d)

Figure 5

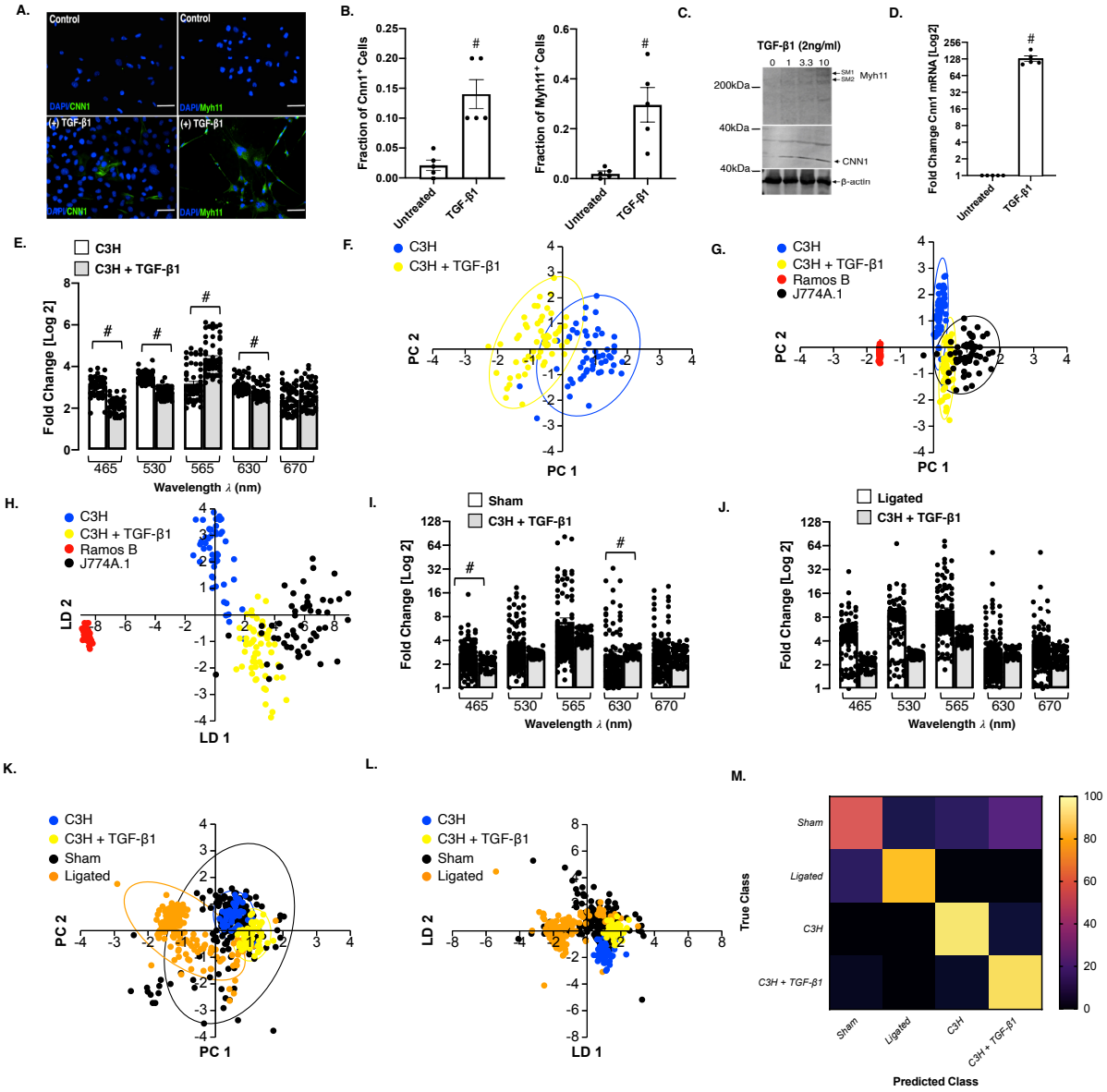
A.
Control
Control
DAPI/CNN1
DAPI/Myh11
(+) TGF-β1
(+) TGF-β1
DAPI/CNN1
DAPI/Myh11
B.
Fraction of Cnn1+ Cells
Fraction of Myh11+ Cells
Untreated
TGF-β1
C.
TGF-β1 (2ng/ml)
0 1 3.3 10
200kDa
40kDa
40kDa
SM1
SM2
Myh11
CNN1
β-actin
D.
Fold Change Cnn1 mRNA [Log2]
Untreated
TGF-β1
E.
C3H
C3H + TGF-β1
Fold Change [Log 2]
465 530 565 630 670
Wavelength λ (nm)
F.
C3H
C3H + TGF-β1
PC 2
PC 1
G.
C3H
C3H + TGF-β1
Ramos B
J774A.1
PC 2
PC 1
H.
C3H
C3H + TGF-β1
Ramos B
J774A.1
LD 2
LD 1
I.
Sham
C3H + TGF-β1
Fold Change [Log 2]
465 530 565 630 670
Wavelength λ (nm)
J.
Ligated
C3H + TGF-β1
Fold Change [Log 2]
465 530 565 630 670
Wavelength λ (nm)
K.
C3H
C3H + TGF-β1
Sham
Ligated
PC 2
PC 1
L.
C3H
C3H + TGF-β1
Sham
Ligated
LD 2
LD 1
M.
True Class
Sham
Ligated
C3H
C3H + TGF-β1
Predicted Class

Figure 6

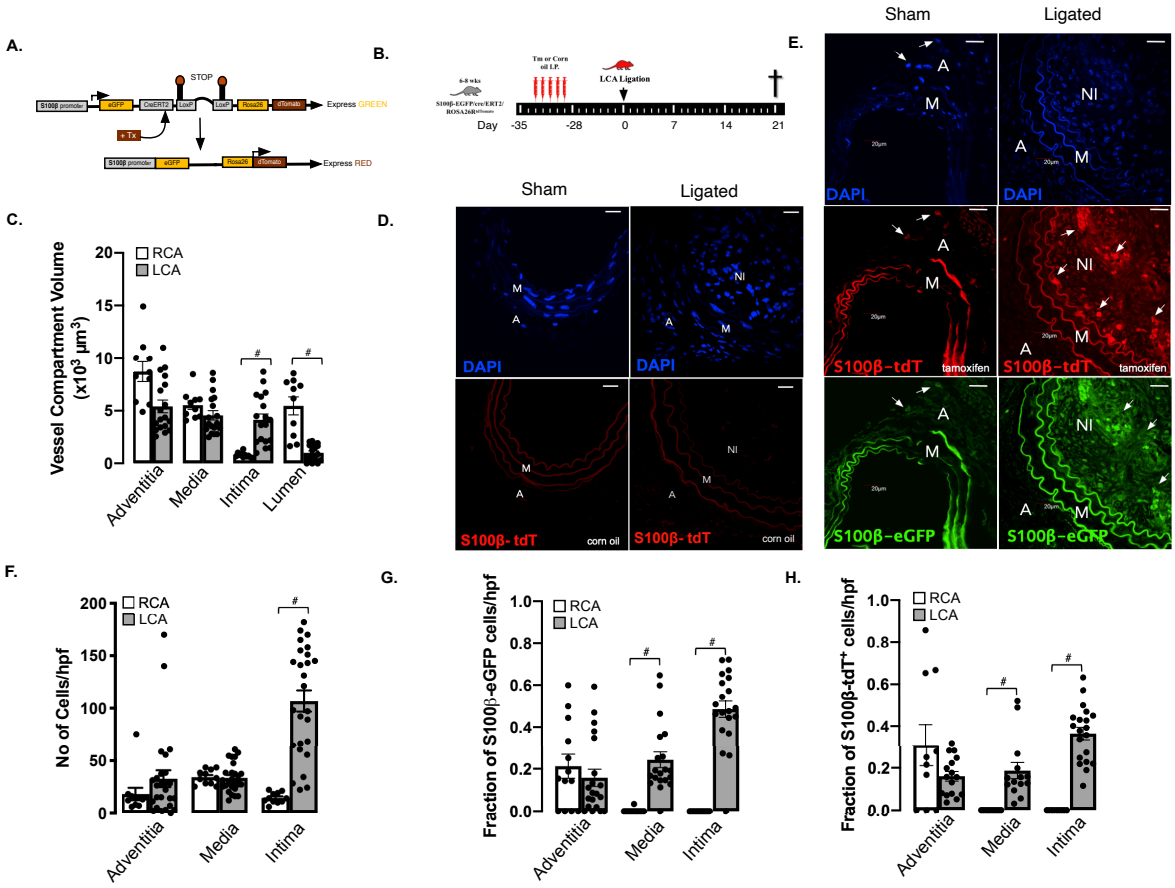
A.
STOP
S100β promoter
eGFP
CreERT2
LoxP
LoxP
Rosa26
dTomato
Express GREEN
+ Tx
S100β promoter
eGFP
Rosa26
dTomato
Express RED
B.
Tm or Corn oil I.P.
LCA Ligation
6-8 wks
S100β-EGFP/cre/ERT2/ROSA26/dTomato
Day
-35
-28
0
7
14
21
C.
Vessel Compartment Volume (x10³ µm³)
RCA
LCA
Adventitia
Media
Intima
Lumen
D.
Sham
Ligated
DAPI
S100β- tdT
corn oil
E.
Sham
Ligated
DAPI
S100β-tdT
tamoxifen
S100β-eGFP
F.
No of Cells/hpf
RCA
LCA
Adventitia
Media
Intima
G.
Fraction of S100β-eGFP cells/hpf
RCA
LCA
Adventitia
Media
Intima
H.
Fraction of S100β-tdT⁺ cells/hpf
RCA
LCA
Adventitia
Media
Intima

Figure 7

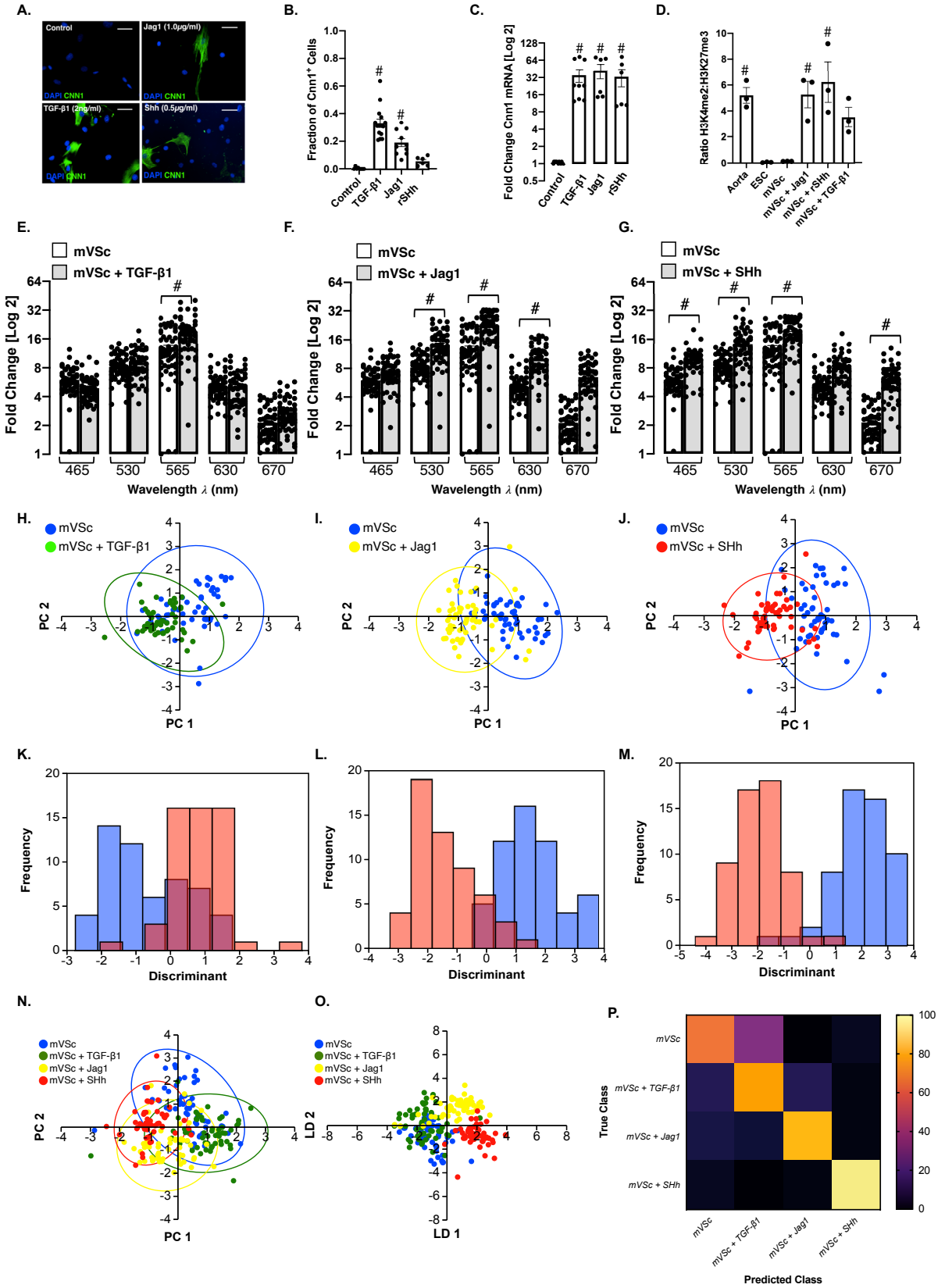
A.
Control
Jag1 (1.0μg/ml)
TGF-β1 (2ng/ml)
Shh (0.5μg/ml)
DAPI CNN1
B.
Fraction of Cnn1+ Cells
Control
TGF-β1
Jag1
rShh
C.
Fold Change Cnn1 mRNA [Log 2]
D.
Ratio H3K4me2:H3K27me3
Aorta
ESC
mVSc
mVSc + Jag1
mVSc + rShh
mVSc + TGF-β1
E.
mVSc
mVSc + TGF-β1
Fold Change [Log 2]
Wavelength λ (nm)
F.
mVSc + Jag1
G.
mVSc + SHh
H.
PC 1
PC 2
I.
J.
K.
Frequency
Discriminant
L.
M.
N.
mVSc + SHh
O.
LD 1
LD 2
P.
True Class
Predicted Class

Figure 8

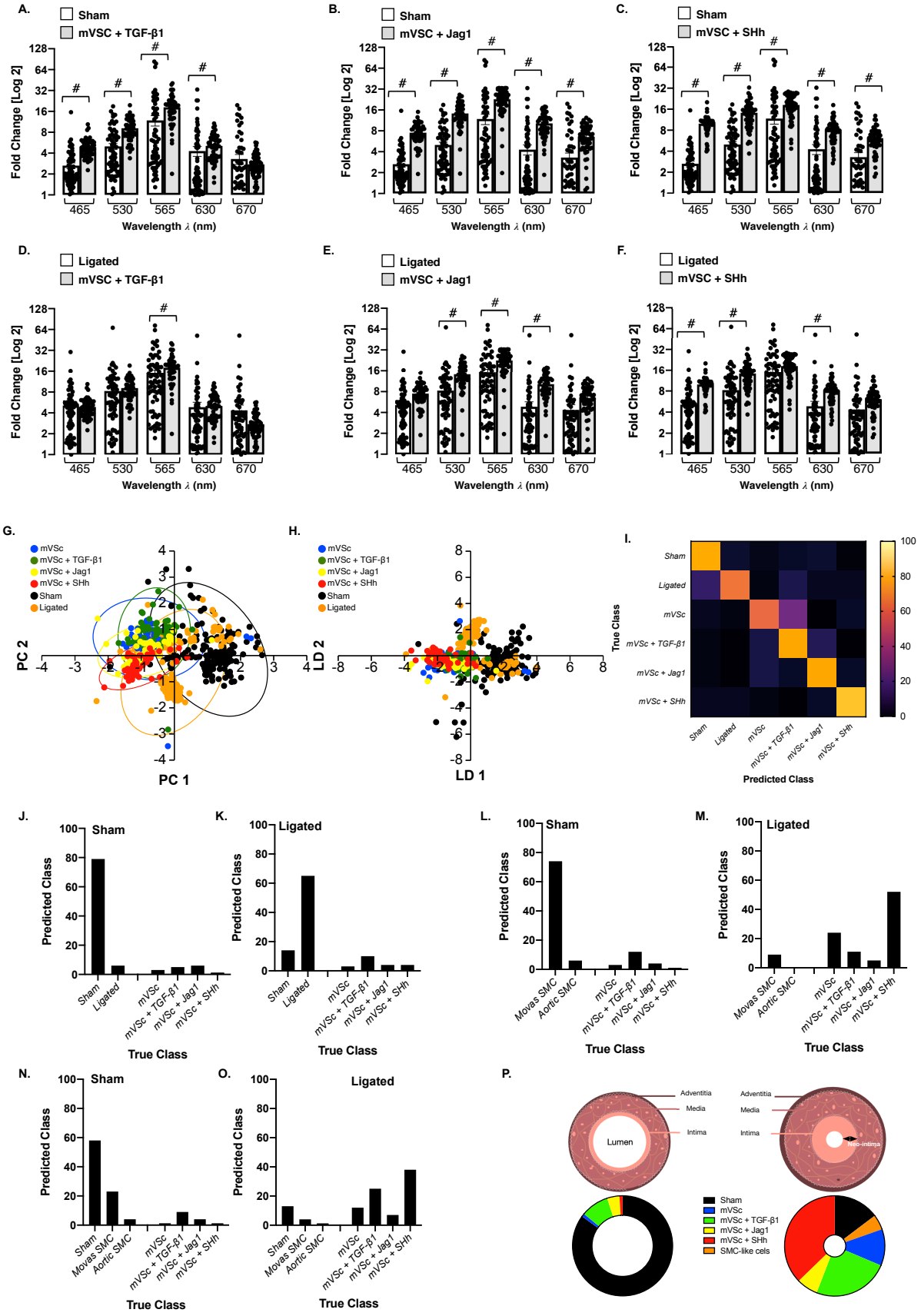
A.
Sham
mVSC + TGF-β1
B.
Sham
mVSC + Jag1
C.
Sham
mVSC + SHh
D.
Ligated
mVSC + TGF-β1
E.
Ligated
mVSC + Jag1
F.
Ligated
mVSC + SHh
Fold Change [Log 2]
Wavelength λ (nm)
465
530
565
630
670
G.
mVSc
mVSc + TGF-β1
mVSc + Jag1
mVSc + SHh
Sham
Ligated
PC 1
PC 2
H.
LD 1
LD 2
I.
True Class
Predicted Class
Sham
Ligated
mVSc
mVSc + TGF-β1
mVSc + Jag1
mVSc + SHh
J.
K.
L.
M.
N.
O.
Predicted Class
True Class
Movas SMC
Aortic SMC
P.
Adventitia
Media
Intima
Lumen
Neo-intima
SMC-like cels

Figure 9

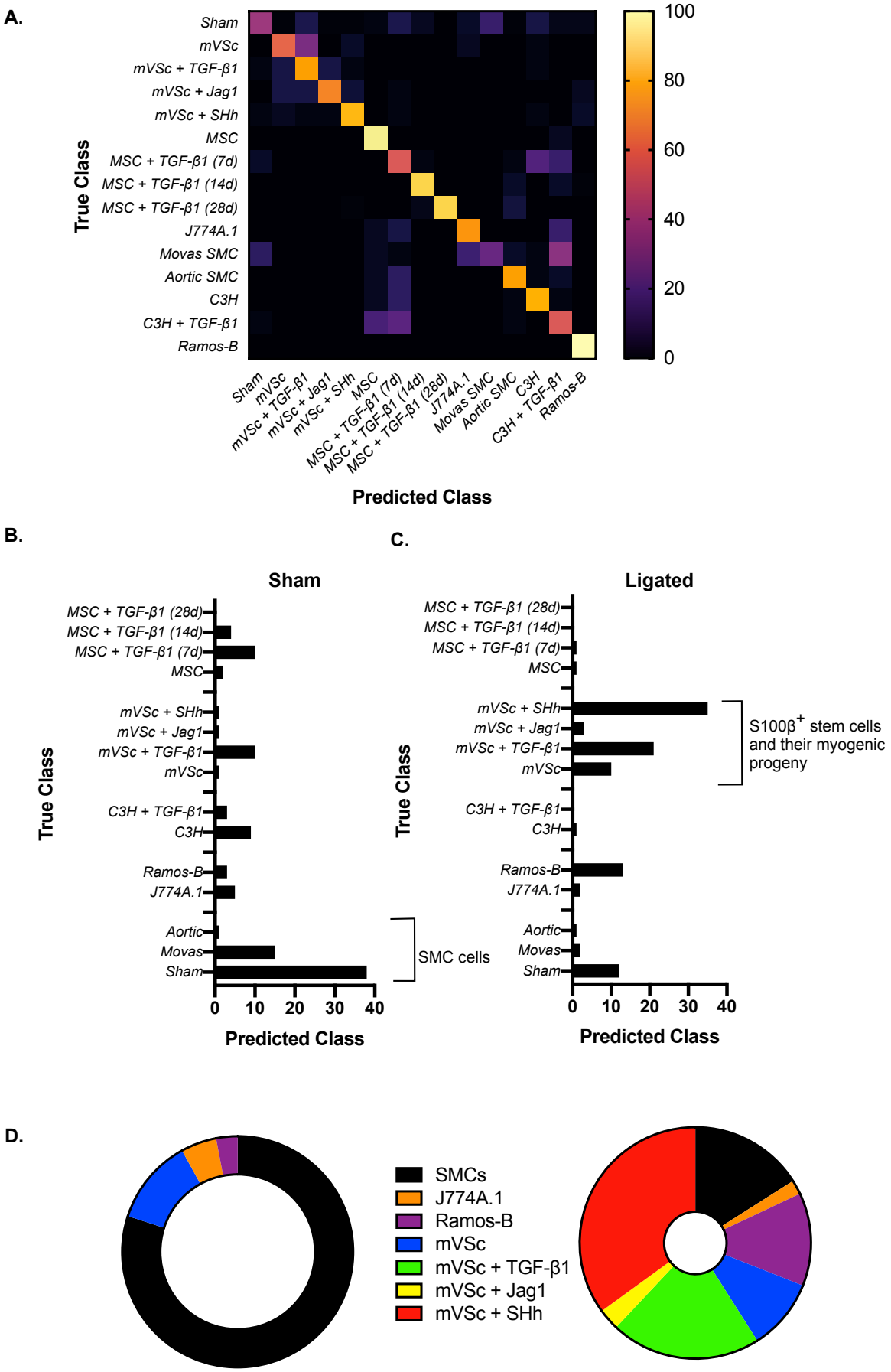
A.
True Class
Predicted Class
Sham
mVSc
mVSc + TGF-β1
mVSc + Jag1
mVSc + SHh
MSC
MSC + TGF-β1 (7d)
MSC + TGF-β1 (14d)
MSC + TGF-β1 (28d)
J774A.1
Movas SMC
Aortic SMC
C3H
C3H + TGF-β1
Ramos-B
100
80
60
40
20
0
B.
Sham
True Class
Predicted Class
0
10
20
30
40
SMC cells
C.
Ligated
True Class
Predicted Class
S100β+ stem cells and their myogenic progeny
D.
SMCs
J774A.1
Ramos-B
mVSc
mVSc + TGF-β1
mVSc + Jag1
mVSc + SHh

Figure 10

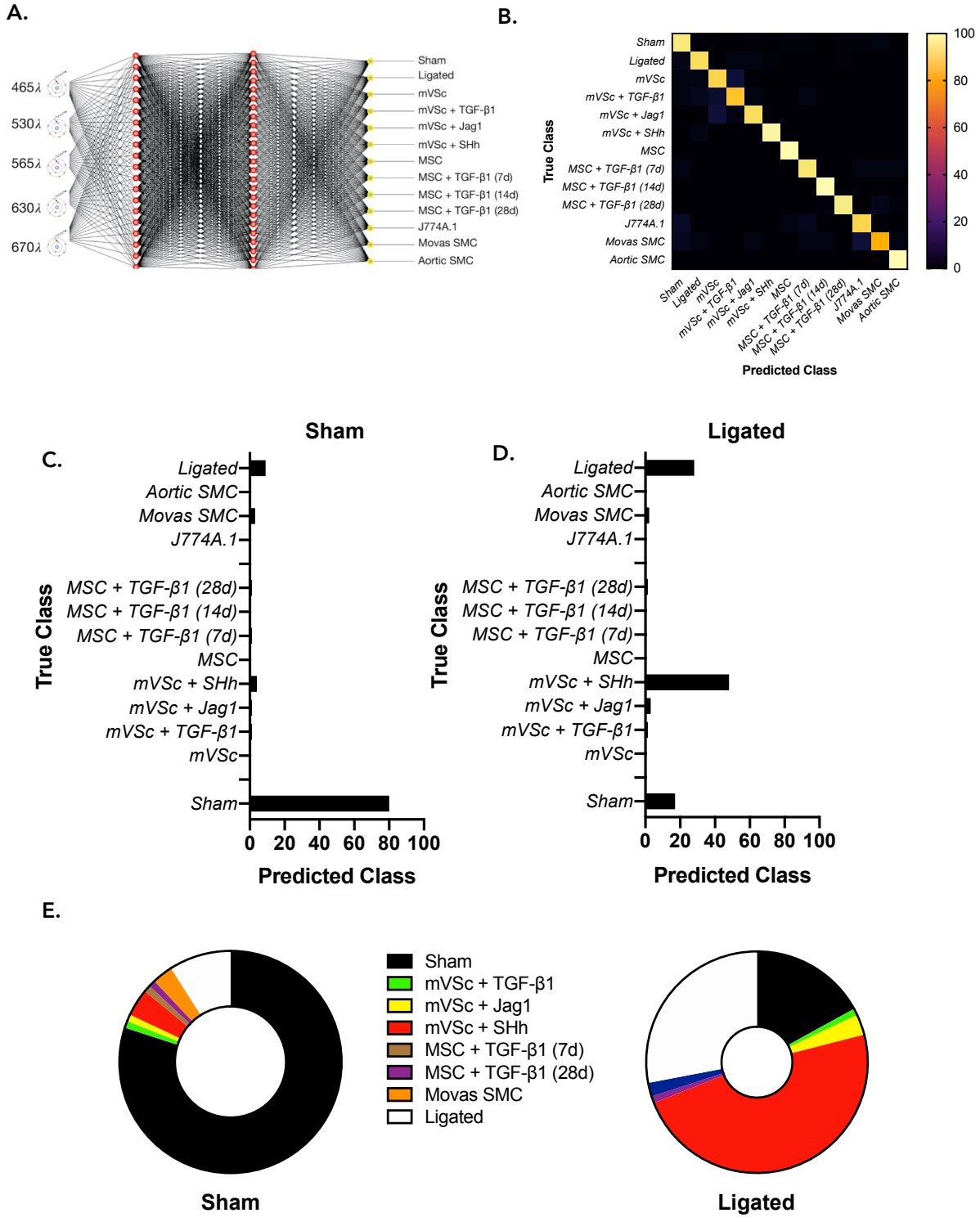
A.
465λ
530λ
565λ
630λ
670λ
Sham
Ligated
mVSc
mVSc + TGF-β1
mVSc + Jag1
mVSc + SHh
MSC
MSC + TGF-β1 (7d)
MSC + TGF-β1 (14d)
MSC + TGF-β1 (28d)
J774A.1
Movas SMC
Aortic SMC
B.
True Class
Predicted Class
100
80
60
40
20
0
C.
Sham
True Class
Predicted Class
0 20 40 60 80 100
D.
Ligated
True Class
Predicted Class
0 20 40 60 80 100
E.
Sham
mVSc + TGF-β1
mVSc + Jag1
mVSc + SHh
MSC + TGF-β1 (7d)
MSC + TGF-β1 (28d)
Movas SMC
Ligated
Sham
Ligated

Figure 11

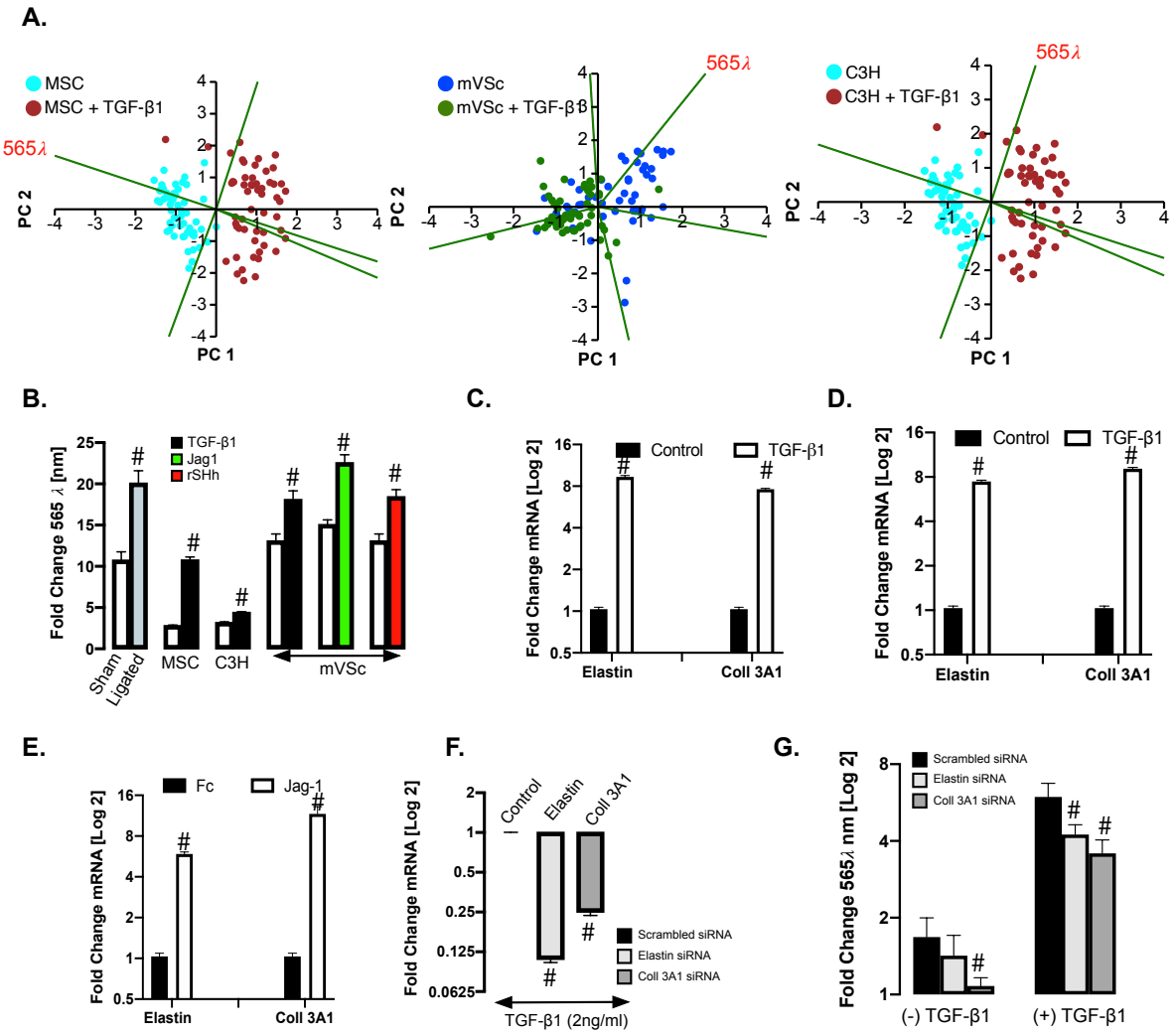
A.
MSC
MSC + TGF-β1
565λ
PC 2
PC 1
mVSc
mVSc + TGF-β1
C3H
C3H + TGF-β1
B.
Fold Change 565 λ [nm]
TGF-β1
Jag1
rSHh
Sham
Ligated
MSC
C3H
mVSc
C.
Fold Change mRNA [Log 2]
Control
TGF-β1
Elastin
Coll 3A1
D.
E.
Fc
Jag-1
F.
Control
Elastin
Coll 3A1
Scrambled siRNA
Elastin siRNA
Coll 3A1 siRNA
TGF-β1 (2ng/ml)
G.
Fold Change 565λ nm [Log 2]
(-) TGF-β1
(+) TGF-β1

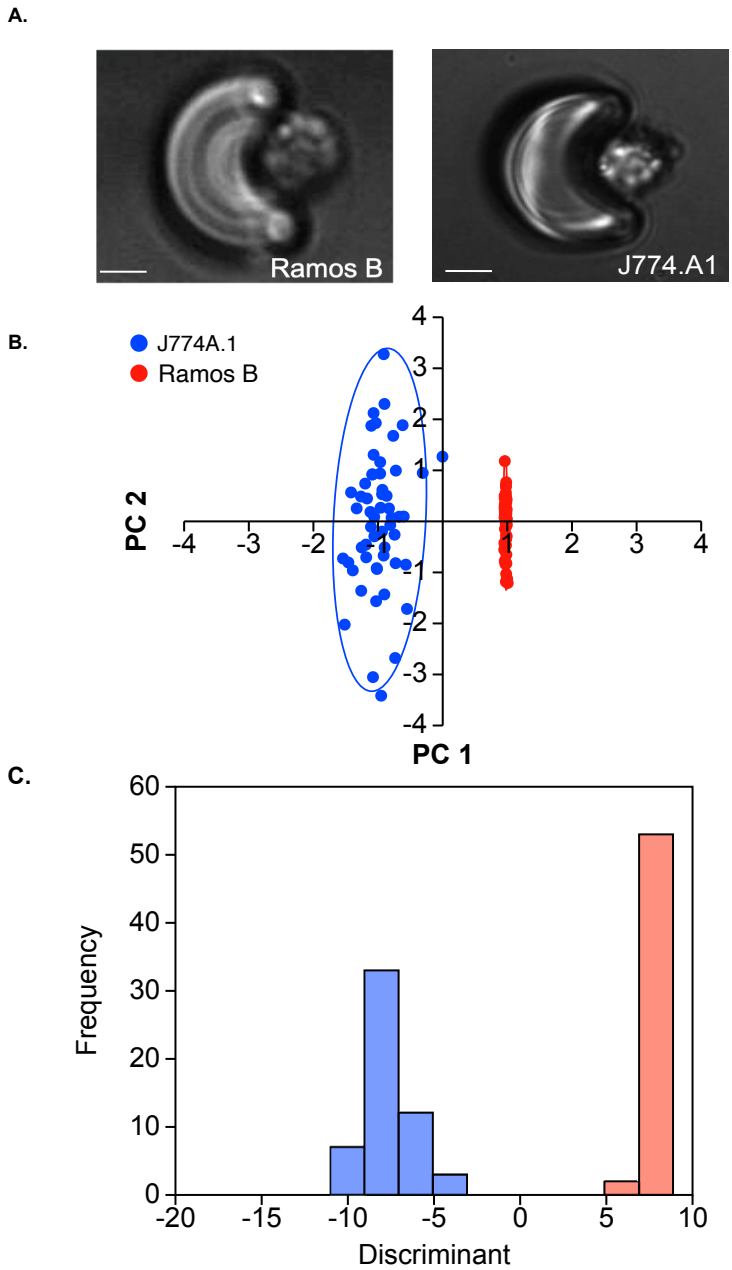

Figure S1 (related to Figure 2).**Single cell photonics of Ramos B and J774A.1 macrophages. A.** Visualisation of Ramos B and J774A.1 cells on each V-cup in the LoaD platform. **B.** PCA loading plots of Ramos B and J774A.1 cells. **C.** LDA of Ramos B and J774A.1 cells. Data are from 55 cells/group over five wavelengths.

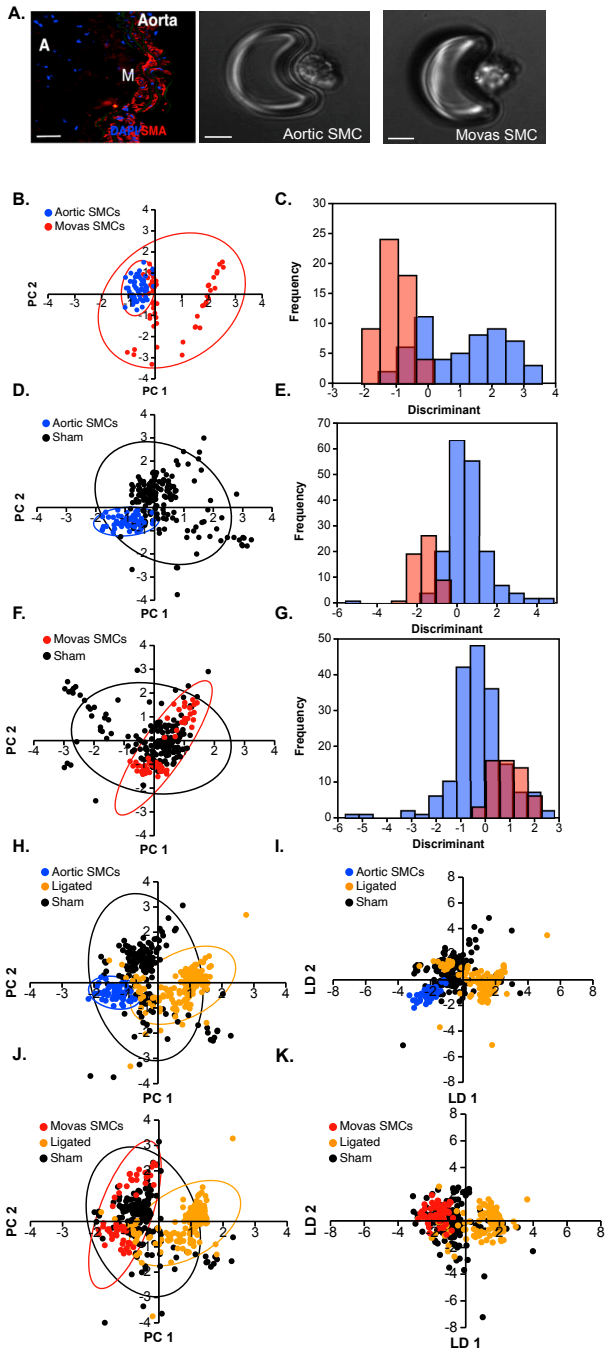

Figure S2 (related to Figure 3).**Single cell photonics of aortic SMCs *ex vivo* and cultured aortic Movas SMC *in vitro*.** **A.** Representative immunohistochemical analysis of α-actin (SMA) expression in mouse aorta and visualisation of aortic SMCs and Movas SMCs on each V-cup in the LoaD platform. **B.** PCA loading plots of aortic SMC and Movas SMCs. **C.** LDA plots of aortic SMC and Movas SMC. Data are from 55 cells/group over five wavelengths. **D.** PCA loading plots of aortic SMCs and carotid artery SMCs (sham). **E.** LDA plots of aortic SMC and sham cells. **F.** PCA loading plots of Movas SMC and carotid artery SMCs (sham). **G.** LDA plots of Movas SMC and sham cells. **H.** PCA loading plots of aortic SMCs, Movas SMCs and sham cells. **I.** LDA plots of aortic SMCs, Movas SMCs and sham cells. **J.** PCA loading plots of aortic SMCs, Movas SMCs and ligated cells. **K.** LDA plots of aortic SMCs, Movas SMCs and ligated cells. Data are from 411 cells across five wavelengths.

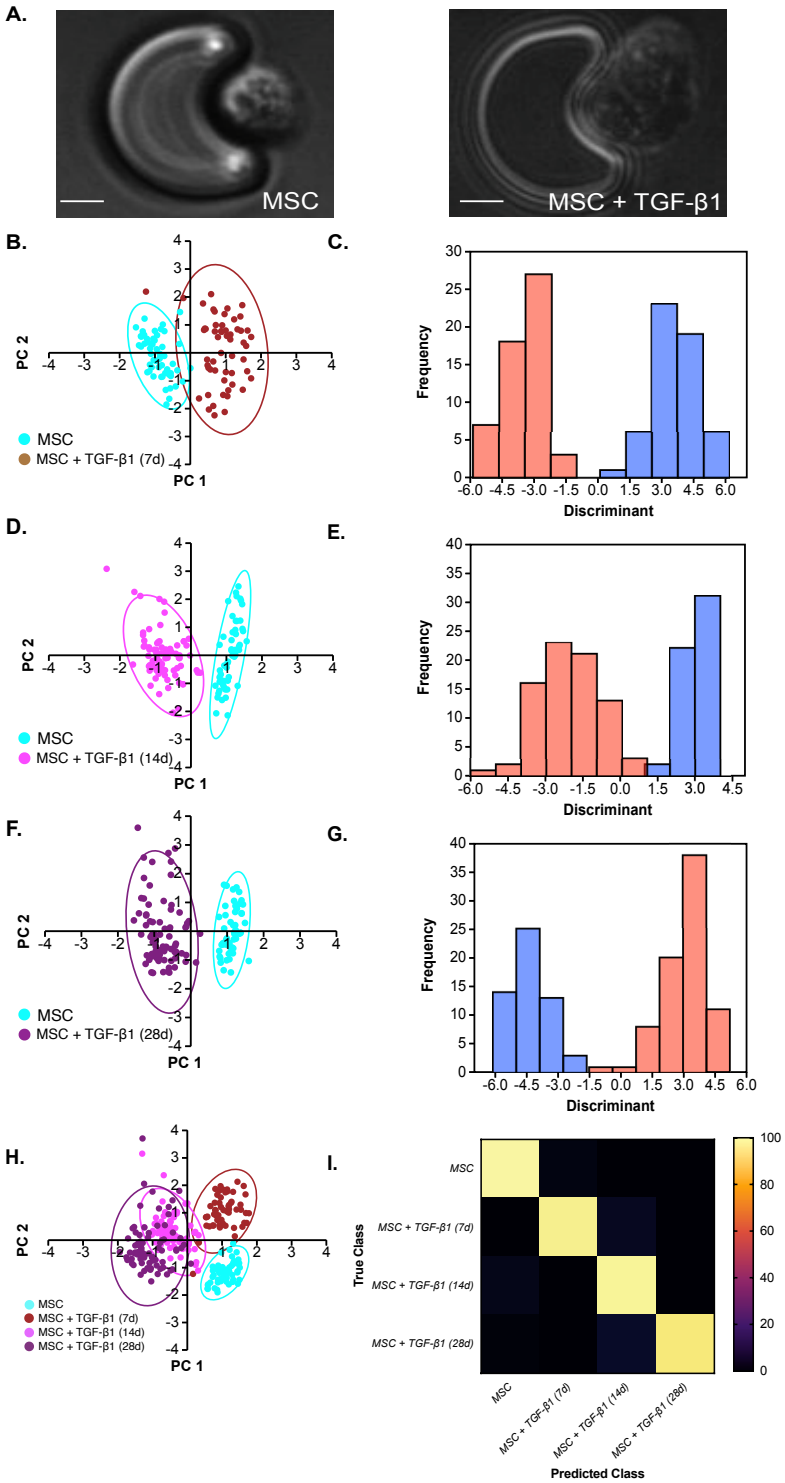

Figure S3 (related to Figure 4). **Single cell photonics of MSC and their myogenic progeny *in vitro*. A.** Visualisation of MSCs and their myogenic progeny on each V-cup in the LoaD platform. **B, D, F.** PCA loading plots of MSCs and MSCs following treatment with TGF-β1 for 7, 14 and 28d. Data are from 55-79 cells/group. **C, E, G.** LDA plots of MSCs and MSCs following treatment with TGF-β1 for 7, 14 and 28d. Data are from 55-79 cells/group. **H.** PCA loading plots of MSC and their myogenic progeny. Data are from 55-79 cells/group. **I.** Confusion matrix of true class and predicted class following a leave-one-out cross-validation procedure using the LDA classifier. Data are from 288 cells across five wavelengths.

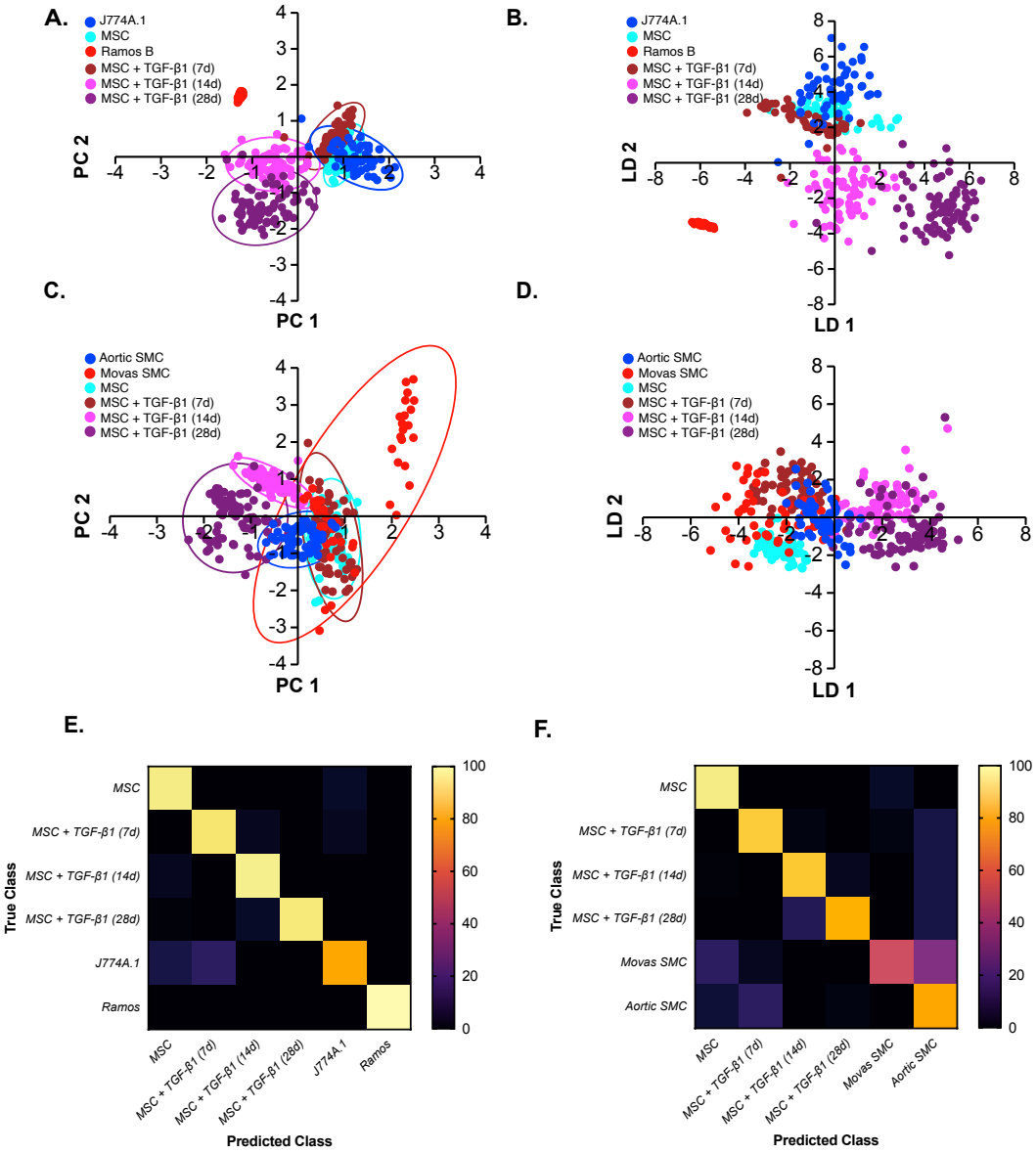

Figure S4 (related to Figure 4). **Single cell photonics of MSC cells and their myogenic progeny compared to aortic SMC, Movas SMC, Ramos B cells and J774A.1 macrophages *in vitro*.** **A.** PCA loading plots of MSCs and their myogenic progeny, Ramos B cells and J774A.1 macrophages. Data are from 55-79 cells/group. **B.** LDA plot of MSCs and their myogenic progeny, Ramos B cells and J774A.1 macrophages. **C.** PCA loading plots of MSCs and their myogenic progeny, aortic SMCs and Movas SMCs. **D.** LDA plots of MSCs and their myogenic progeny, aortic SMCs and Movas SMCs. Data are from 55-79 cells/group. **E.** Confusion matrix of true class and predicted class following a leave-one-out cross-validation procedure using the LDA classifier. Data are from 378 cells across five wavelengths. **F.** Confusion matrix of true class and predicted class following a leave-one-out cross-validation procedure using the LDA classifier. Data are from 378 cells across five wavelengths.

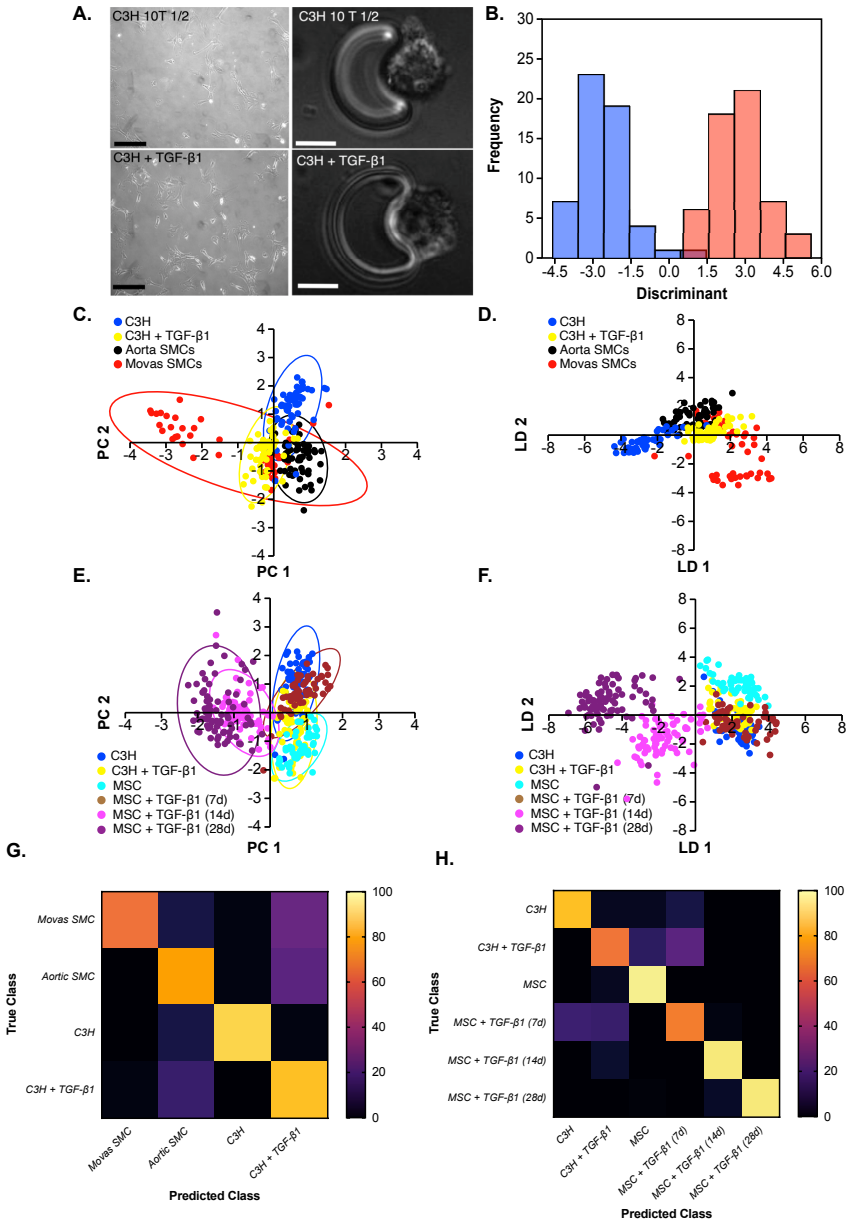

Figure S5 (related to Figure 5). **Single cell photonics of C3H10T1/2 cells and their myogenic progeny compared to aortic SMC, Movas SMC and MSC and their myogenic progeny *in vitro*.** **A.** Visualisation of C3H10T1/2 cells and their myogenic progeny on each V-cup in the LoaD platform. **B.** LDA plot of C3H10T1/2 cells before and after treatment with TGF-β1 (2ng/ml) for 7 d. Data are from 55 cells/group. **C.** PCA loading plots of C3H10T1/2 cells and their myogenic progeny, aortic SMCs and Movas SMCs. Data are from 55 cells/group. **D.** LDA plots of C3H10T1/2 cells and their myogenic progeny, aortic SMCs and Movas SMCs. **E.** PCA loading plots of C3H10T1/2 cells and their myogenic progeny, MSCs and their myogenic progeny. Data are from 55-79 cells/group. **F.** LDA plots of C3H10T1/2 cells and their myogenic progeny, MSCs and their myogenic progeny. **G.** Confusion matrix of true class and predicted class following a leave-one-out cross-validation procedure using the LDA classifier. Data are from 220 cells across five wavelengths. **H.** Confusion matrix of true class and predicted class following a leave-one-out cross-validation procedure using the LDA classifier. Data are from 367 cells across five wavelengths

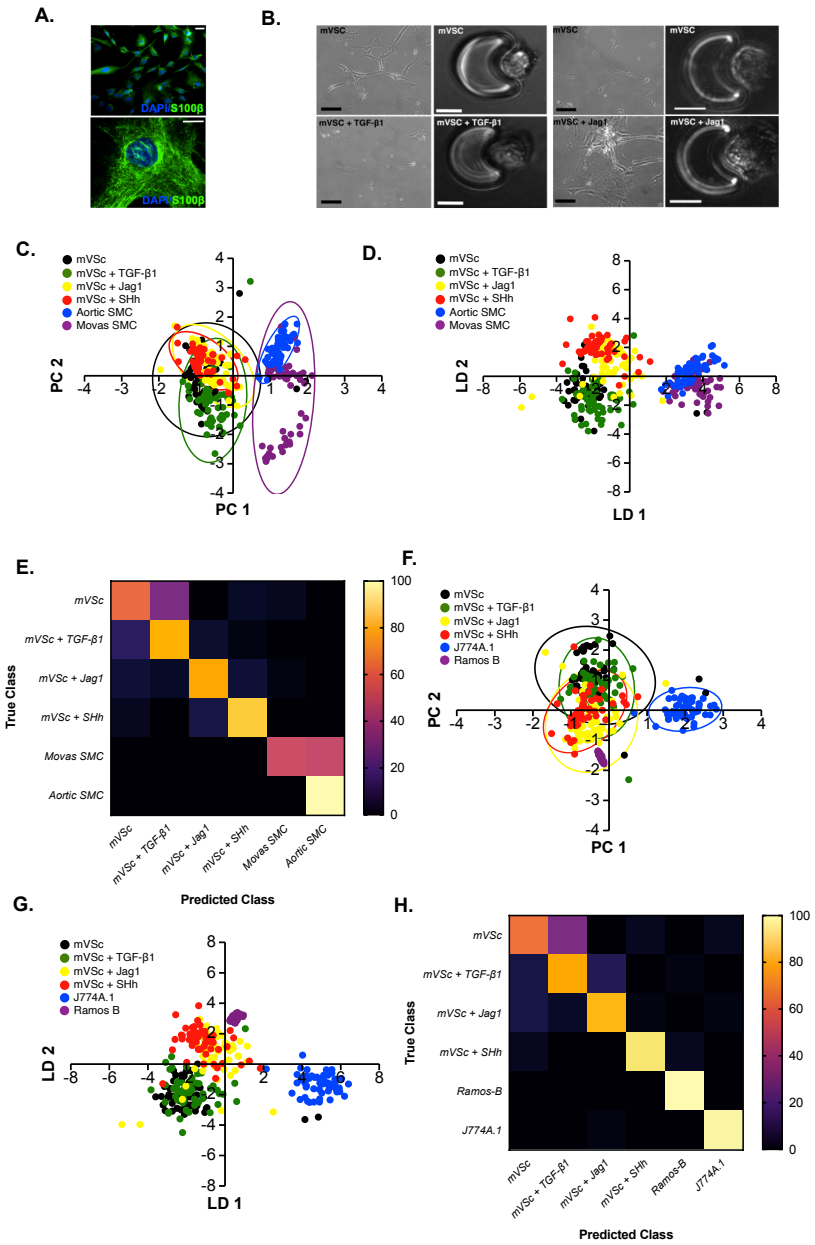

Figure S6 (related to Figure 6). **Single cell photonics of mVSc and their myogenic progeny compared to aortic SMC, Movas SMC, Ramos B and J774A.1 macrophages.** **A.** Representative immunocytochemical analysis of S100β expression in mVSc. **B.** Visualisation of mVSc and their myogenic progeny on each V-cup in the LoaD platform. **C.** PCA loading plots of mVSc and their myogenic progeny, aortic SMCs and Movas SMCs. Data are from 55 cells/group. **D.** LDA plot of mVSc and their myogenic progeny, aortic SMCs and Movas SMCs. Data are from 55 cells/group. **E.** Confusion matrix of true class and predicted class following a leave-one-out cross-validation procedure using the LDA classifier. Data are from 319 cells across five wavelengths. **F.** PCA loading plots of mVSc and their myogenic progeny, Ramos B cells and J774A.1 macrophages. Data are from 55 cells/group. **G.** LDA plot of mVSc and their myogenic progeny, Ramos B cells and J774A.1 macrophages. Data are from 55 cells/group. **H.** Confusion matrix of true class and predicted class following a leave-one-out cross-validation procedure using the LDA classifier. Data are from 319 cells across five wavelengths.

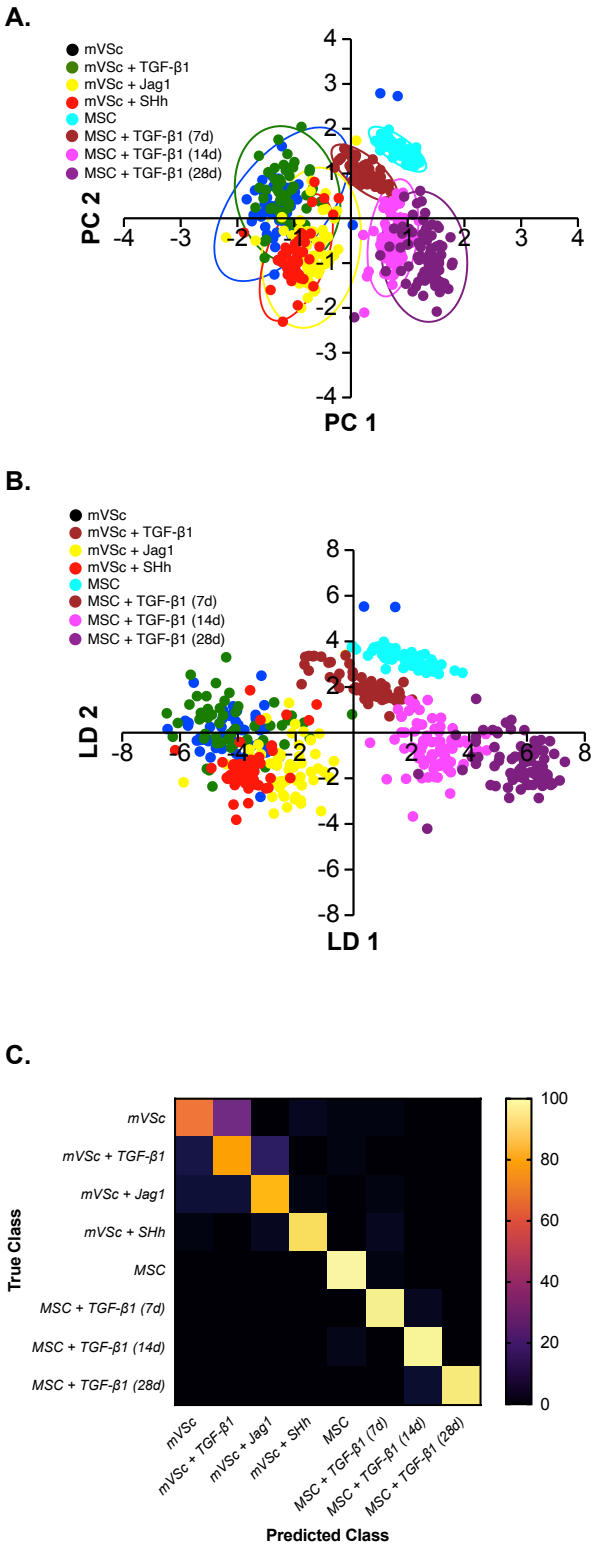

Figure S7 (related to Figure 6). **Single cell photonics of mVSc and their myogenic progeny compared to MSCs and their myogenic progeny. A.** PCA loading plots of mVSc and their myogenic progeny, and MSC and their myogenic progeny. Data are from 55-79 cells/group. **B.** LDA plot of mVSc and their myogenic progeny, and MSC and their myogenic progeny. Data are from 55-79 cells/group. **C.** Confusion matrix of true class and predicted class following a leave-one-out cross-validation procedure using the LDA classifier. Data are from 487 cells across five wavelengths.

References

1. Virani, S. S. *et al.* Heart Disease and Stroke Statistics—2020 Update: A Report From the American Heart Association. *Circulation* **141**, e139–e596 (2020).
2. Bennett, M. R., Sinha, S. & Owens, G. K. Vascular Smooth Muscle Cells in Atherosclerosis. *Circ. Res.* **118**, 692–702 (2016).
3. Sakamoto, A. *et al.* Pathologic intimal thickening: Are we any closer to understand early transitional plaques that lead to symptomatic disease? *Atherosclerosis* **274**, 227–229 (2018).
4. Halcox, J. P. J. *et al.* Endothelial Function Predicts Progression of Carotid Intima-Media Thickness. *Circulation* **119**, 1005–1012 (2009).
5. Hromada, C., Mühleder, S., Grillari, J., Redl, H. & Holnthoner, W. Endothelial Extracellular Vesicles-Promises and Challenges. *Front. Physiol.* **8**, 275 (2017).
6. Zhang, C., Zeng, L., Emanueli, C. & Xu, Q. Blood flow and stem cells in vascular disease. *Cardiovasc. Res.* **99**, 251–259 (2013).
7. Korshunov, V. A. & Berk, B. C. Flow-induced vascular remodeling in the mouse: a model for carotid intima-media thickening. *Arterioscler. Thromb. Vasc. Biol.* **23**, 2185–91 (2003).
8. Liu, W., Redmond, E. M., Morrow, D. & Cullen, J. P. Differential effects of daily-moderate versus weekend-binge alcohol consumption on atherosclerotic plaque development in mice. *Atherosclerosis* **219**, 448–54 (2011).
9. Nam, D. *et al.* Partial carotid ligation is a model of acutely induced disturbed flow, leading to rapid endothelial dysfunction and atherosclerosis. *Am. J. Physiol. Heart Circ. Physiol.* **297**, H1535-43 (2009).
10. Nemenoff, R. A. *et al.* SDF-1α induction in mature smooth muscle cells by inactivation of PTEN is a critical mediator of exacerbated injury-induced neointima formation. *Arterioscler. Thromb. Vasc. Biol.* **31**, 1300–8 (2011).
11. Chappell, J. *et al.* Extensive Proliferation of a Subset of Differentiated, yet Plastic, Medial Vascular Smooth Muscle Cells Contributes to Neointimal Formation in Mouse Injury and Atherosclerosis Models. *Circ. Res.* **119**, 1313–1323 (2016).
12. Herring, B., Hoggatt, A. M., Burlak, C. & Offermanns, S. Previously differentiated medial vascular smooth muscle cells contribute to neointima formation following vascular injury. *Vasc. Cell* **6**, 21 (2014).
13. Shankman, L. S. *et al.* KLF4-dependent phenotypic modulation of smooth muscle cells has a key role in atherosclerotic plaque pathogenesis. *Nat. Med.* **21**, 628–637 (2015).
14. Shi, N., Mei, X. & Chen, S.-Y. Smooth Muscle Cells in Vascular Remodeling. *Arterioscler. Thromb. Vasc. Biol.* **39**, (2019).
15. Baker, A. H. & Péault, B. A Gli(1)ttering Role for Perivascular Stem Cells in Blood Vessel Remodeling. *Cell Stem Cell* **19**, 563–565 (2016).
16. Kramann, R. *et al.* Adventitial MSC-like Cells Are Progenitors of Vascular Smooth Muscle Cells and Drive Vascular Calcification in Chronic Kidney Disease. *Cell Stem Cell* **19**, 628–642 (2016).
17. Majesky, M. W. *et al.* Differentiated Smooth Muscle Cells Generate a Subpopulation of Resident Vascular Progenitor Cells in the Adventitia Regulated by Klf4. *Circ. Res.* **120**, 296–311 (2017).
18. Schneider, R. K. *et al.* Gli1+ Mesenchymal Stromal Cells Are a Key Driver of Bone Marrow Fibrosis and an Important Cellular Therapeutic Target. *Cell Stem Cell* **23**, 308–

309 (2018).
19. Wan, M. *et al.* Injury-activated transforming growth factor β controls mobilization of mesenchymal stem cells for tissue remodeling. *Stem Cells* **30**, 2498–511 (2012).
20. Yuan, F. *et al.* Contribution of Vascular Cells to Neointimal Formation. *PLoS One* **12**, e0168914 (2017).
21. Dobnikar, L. *et al.* Disease-relevant transcriptional signatures identified in individual smooth muscle cells from healthy mouse vessels. *Nat. Commun.* **9**, 4567 (2018).
22. Tang, J. *et al.* Arterial Sca1+ Vascular Stem Cells Generate De Novo Smooth Muscle for Artery Repair and Regeneration. *Cell Stem Cell* **26**, 81-96.e4 (2020).
23. Chen, S. & Lechleider, R. J. Transforming Growth Factor-β-Induced Differentiation of Smooth Muscle From a Neural Crest Stem Cell Line. *Circ. Res.* **94**, 1195–1202 (2004).
24. Majesky, M. W., Lindner, V., Twardzik, D. R., Schwartz, S. M. & Reidy, M. A. Production of transforming growth factor beta 1 during repair of arterial injury. *J. Clin. Invest.* **88**, 904–910 (1991).
25. Schulick, A. H. *et al.* Overexpression of transforming growth factor beta1 in arterial endothelium causes hyperplasia, apoptosis, and cartilaginous metaplasia. *Proc. Natl. Acad. Sci. U. S. A.* **95**, 6983–8 (1998).
26. Chen, P.-Y. *et al.* Endothelial TGF-β signalling drives vascular inflammation and atherosclerosis. *Nat. Metab.* **1**, 912–926 (2019).
27. Bobik, A. Transforming Growth Factor-βs and Vascular Disorders. *Arterioscler. Thromb. Vasc. Biol.* **26**, 1712–1720 (2006).
28. Pang, L. *et al.* TGF-β1/Smad signaling, MMP-14, and MSC markers in arterial injury: discovery of the molecular basis of restenosis. *Int. J. Clin. Exp. Pathol.* **7**, 2915–24 (2014).
29. López-Mejías, R. *et al.* Influence of coronary artery disease and subclinical atherosclerosis related polymorphisms on the risk of atherosclerosis in rheumatoid arthritis. *Sci. Rep.* **7**, 40303 (2017).
30. Aravani, D. *et al. HHIPL1* , a Gene at the 14q32 Coronary Artery Disease Locus, Positively Regulates Hedgehog Signaling and Promotes Atherosclerosis. *Circulation* **140**, 500–513 (2019).
31. Wu, X. *et al.* Role of Jagged1 in Arterial Lesions After Vascular Injury. *Arterioscler. Thromb. Vasc. Biol.* **31**, 2000–2006 (2011).
32. Redmond, E. M. *et al.* Inhibition of Patched-1 Prevents Injury-Induced Neointimal Hyperplasia. *Arterioscler. Thromb. Vasc. Biol.* **33**, 1960–1964 (2013).
33. Shaw, T. J. A Notch in our understanding of vascular disease. *Sci. Transl. Med.* **7**, 315ec204-315ec204 (2015).
34. Doi, H. *et al.* Notch signaling regulates the differentiation of bone marrow-derived cells into smooth muscle-like cells during arterial lesion formation. *Biochem. Biophys. Res. Commun.* **381**, 654–659 (2009).
35. Tian, D.-Y., Jin, X.-R., Zeng, X. & Wang, Y. Notch Signaling in Endothelial Cells: Is It the Therapeutic Target for Vascular Neointimal Hyperplasia? *Int. J. Mol. Sci.* **18**, 1615 (2017).
36. Redmond, E. M. *et al.* Perivascular Delivery of Notch 1 siRNA Inhibits Injury-Induced Arterial Remodeling. *PLoS One* **9**, e84122 (2014).
37. Alyass, A., Turcotte, M. & Meyre, D. From big data analysis to personalized medicine for all: challenges and opportunities. *BMC Med. Genomics* **8**, 33 (2015).
38. Peng, L. *et al.* Single-cell RNA-seq clustering: datasets, models, and algorithms. *RNA*

Biol. 1–19 (2020) doi:10.1080/15476286.2020.1728961.
39. Liu, M. & Gomez, D. Smooth Muscle Cell Phenotypic Diversity. *Arterioscler. Thromb. Vasc. Biol.* **39**, 1715–1723 (2019).
40. Qavi, A. J., Washburn, A. L., Byeon, J.-Y. & Bailey, R. C. Label-free technologies for quantitative multiparameter biological analysis. *Anal. Bioanal. Chem.* **394**, 121–135 (2009).
41. Amiri, I. S. *et al.* Introduction to photonics: Principles and the most recent applications of microstructures. *Micromachines* vol. 9 (2018).
42. Monici, M. Cell and tissue autofluorescence research and diagnostic applications. *Biotechnol. Annu. Rev.* **11**, 227–256 (2005).
43. Croce, A. C., Ferrigno, A., Bottiroli, G. & Vairetti, M. Autofluorescence-based optical biopsy: An effective diagnostic tool in hepatology. *Liver Int.* **38**, 1160–1174 (2018).
44. Chacko, J. V. & Eliceiri, K. W. Autofluorescence lifetime imaging of cellular metabolism: Sensitivity toward cell density, pH, intracellular, and intercellular heterogeneity. *Cytom. Part A* **95**, 56–69 (2019).
45. Burger, R. *et al.* Array-based capture, distribution, counting and multiplexed assaying of beads on a centrifugal microfluidic platform. *Lab Chip* **12**, 1289–95 (2012).
46. Burger, R. *et al.* An integrated centrifugo-opto-microfluidic platform for arraying, analysis, identification and manipulation of individual cells. *Lab Chip* **15**, 378–381 (2015).
47. King, D. *et al.* Label-Free Multi Parameter Optical Interrogation of Endothelial Activation in Single Cells using a Lab on a Disc Platform. *Sci. Rep.* **9**, 4157 (2019).
48. Sidey-Gibbons, J. A. M. & Sidey-Gibbons, C. J. Machine learning in medicine: a practical introduction. *BMC Med. Res. Methodol.* **19**, 64 (2019).
49. Pradhan, P., Guo, S., Ryabchykov, O., Popp, J. & Bocklitz, T. W. Deep learning a boon for biophotonics? *Journal of Biophotonics* e201960186 (2020) doi:10.1002/jbio.201960186.
50. Wiles, E. T. & Selker, E. U. H3K27 methylation: a promiscuous repressive chromatin mark. *Curr. Opin. Genet. Dev.* **43**, 31–37 (2017).
51. NINOMIYA, K., TAKAHASHI, A., FUJIOKA, Y., ISHIKAWA, Y. & YOKOYAMA, M. Transforming Growth Factor-.BETA. Signaling Enhances Transdifferentiation of Macrophages into Smooth Muscle-Like Cells. *Hypertens. Res.* **29**, 269–276 (2006).
52. Frank, E., Hall, M., Trigg, L., Holmes, G. & Witten, I. H. Data mining in bioinformatics using Weka. *Bioinformatics* **20**, 2479–81 (2004).
53. Hammer, Ø., Harper, D. A. T. & Ryan, P. D. Past: Paleontological statistics software package for education and data analysis. *Palaeontol. Electron.* **4**, 178 (2001).
54. Jiang, X., Rowitch, D. H., Soriano, P., McMahon, A. P. & Sucov, H. M. Fate of the mammalian cardiac neural crest. *Development* **127**, 1607–16 (2000).
55. Esner, M. *et al.* Smooth muscle of the dorsal aorta shares a common clonal origin with skeletal muscle of the myotome. *Development* **133**, 737–49 (2006).
56. Miwa, H. & Era, T. Tracing the destiny of mesenchymal stem cells from embryo to adult bone marrow and white adipose tissue via Pdgfrα expression. *Development* **145**, dev155879 (2018).
57. Hirschi, K. K., Rohovsky, S. A. & D'Amore, P. A. PDGF, TGF-beta, and heterotypic cell-cell interactions mediate endothelial cell-induced recruitment of 10T1/2 cells and their differentiation to a smooth muscle fate. *J. Cell Biol.* **141**, 805–14 (1998).
58. Molony, C. *et al.* Label-free discrimination analysis of de-differentiated vascular

smooth muscle cells, mesenchymal stem cells and their vascular and osteogenic progeny using vibrational spectroscopy. *Biochim. Biophys. acta. Mol. cell Res.* **1865**, 343–353 (2018).
59. Tang, Z. *et al.* Differentiation of multipotent vascular stem cells contributes to vascular diseases. *Nat. Commun.* **3**, 875 (2012).
60. Kennedy, E. *et al.* Embryonic rat vascular smooth muscle cells revisited - a model for neonatal, neointimal SMC or differentiated vascular stem cells? *Vasc. Cell* **6**, 6 (2014).
61. Kennedy, E. *et al.* Adult vascular smooth muscle cells in culture express neural stem cell markers typical of resident multipotent vascular stem cells. *Cell Tissue Res.* **358**, 203–16 (2014).
62. Murry, C. E., Gipaya, C. T., Bartosek, T., Benditt, E. P. & Schwartz, S. M. Monoclonality of smooth muscle cells in human atherosclerosis. *Am. J. Pathol.* **151**, 697–705 (1997).
63. Basatemur, G. L., Jørgensen, H. F., Clarke, M. C. H., Bennett, M. R. & Mallat, Z. Vascular smooth muscle cells in atherosclerosis. *Nat. Rev. Cardiol.* **16**, 727–744 (2019).
64. Gomez, D. & Owens, G. K. Reconciling Smooth Muscle Cell Oligoclonality and Proliferative Capacity in Experimental Atherosclerosis. *Circ. Res.* **119**, 1262–1264 (2016).
65. Hoglund, V. J., Dong, X. R. & Majesky, M. W. Neointima formation: a local affair. *Arterioscler. Thromb. Vasc. Biol.* **30**, 1877–9 (2010).
66. Campbell, J. H. & Campbell, G. R. Smooth Muscle Phenotypic Modulation—A Personal Experience. *Arterioscler. Thromb. Vasc. Biol.* **32**, 1784–1789 (2012).
67. Nguyen, A. T. *et al.* Smooth muscle cell plasticity: fact or fiction? *Circ. Res.* **112**, 17–22 (2013).
68. Cooley, B. C. *et al.* TGF- Signaling Mediates Endothelial-to-Mesenchymal Transition (EndMT) During Vein Graft Remodeling. *Sci. Transl. Med.* **6**, 227ra34-227ra34 (2014).
69. Zhang, L., Issa Bhaloo, S., Chen, T., Zhou, B. & Xu, Q. Role of Resident Stem Cells in Vessel Formation and Arteriosclerosis. *Circ. Res.* **122**, 1608–1624 (2018).
70. Roostalu, U. *et al.* Distinct Cellular Mechanisms Underlie Smooth Muscle Turnover in Vascular Development and Repair. *Circ. Res.* **122**, 267–281 (2018).
71. Owens, G. K. Molecular control of vascular smooth muscle cell differentiation and phenotypic plasticity. *Novartis Found. Symp.* **283**, 174–91; discussion 191-3, 238–41 (2007).
72. Chakraborty, R. *et al.* Promoters to Study Vascular Smooth Muscle. *Arterioscler. Thromb. Vasc. Biol.* **39**, 603–612 (2019).
73. Murgai, M. *et al.* KLF4-dependent perivascular cell plasticity mediates pre-metastatic niche formation and metastasis. *Nat. Med.* **23**, 1176–1190 (2017).
74. Sheikh, A. Q., Lighthouse, J. K. & Greif, D. M. Recapitulation of Developing Artery Muscularization in Pulmonary Hypertension. *Cell Rep.* **6**, 809–817 (2014).
75. Beckers, L. *et al.* Disruption of hedgehog signalling in ApoE - /- mice reduces plasma lipid levels, but increases atherosclerosis due to enhanced lipid uptake by macrophages. *J. Pathol.* **212**, 420–8 (2007).
76. Ali, H. *et al.* Localization and characterization of a novel secreted protein, SCUBE2, in the development and progression of atherosclerosis. *Kobe J. Med. Sci.* **59**, E122-31 (2013).
77. Dutzmann, J. *et al.* Sonic hedgehog-dependent activation of adventitial fibroblasts promotes neointima formation. *Cardiovasc. Res.* **113**, 1653–1663 (2017).

78. Morrow, D. *et al.* Sonic Hedgehog induces Notch target gene expression in vascular smooth muscle cells via VEGF-A. *Arterioscler. Thromb. Vasc. Biol.* **29**, 1112–8 (2009).
79. Li, F. *et al.* Sonic hedgehog signaling induces vascular smooth muscle cell proliferation via induction of the G1 cyclin-retinoblastoma axis. *Arterioscler. Thromb. Vasc. Biol.* **30**, 1787–94 (2010).
80. Wang, G. *et al.* Activation of the sonic hedgehog signaling controls human pulmonary arterial smooth muscle cell proliferation in response to hypoxia. *Biochim. Biophys. Acta* **1803**, 1359–67 (2010).
81. Passman, J. N. *et al.* A sonic hedgehog signaling domain in the arterial adventitia supports resident Sca1+ smooth muscle progenitor cells. *Proc. Natl. Acad. Sci. U. S. A.* **105**, 9349–54 (2008).
82. Shikatani, E. A. *et al.* c-Myb Regulates Proliferation and Differentiation of Adventitial Sca1+ Vascular Smooth Muscle Cell Progenitors by Transactivation of Myocardin. *Arterioscler. Thromb. Vasc. Biol.* **36**, 1367–76 (2016).
83. Tsai, T.-N. *et al.* Contribution of stem cells to neointimal formation of decellularized vessel grafts in a novel mouse model. *Am. J. Pathol.* **181**, 362–73 (2012).
84. Fitzpatrick, E. *et al.* Alcohol Reduces Arterial Remodeling by Inhibiting Sonic Hedgehog-Stimulated Stem Cell Antigen-1 Positive Progenitor Stem Cell Expansion. *Alcohol. Clin. Exp. Res.* **41**, 2051–2065 (2017).
85. Godinez, W. J., Hossain, I., Lazic, S. E., Davies, J. W. & Zhang, X. A multi-scale convolutional neural network for phenotyping high-content cellular images. *Bioinformatics* **33**, 2010–2019 (2017).
86. Wang, Z. J., Walsh, A. J., Skala, M. C. & Gitter, A. Classifying T cell activity in autofluorescence intensity images with convolutional neural networks. *J. Biophotonics* **13**, (2020).
87. Yoon, J. *et al.* Identification of non-activated lymphocytes using three-dimensional refractive index tomography and machine learning. *Sci. Rep.* **7**, 1–10 (2017).
88. Kusumoto, D. *et al.* Automated Deep Learning-Based System to Identify Endothelial Cells Derived from Induced Pluripotent Stem Cells. *Stem Cell Reports* **10**, 1687–1695 (2018).
89. Buggenthin, F. *et al.* Prospective identification of hematopoietic lineage choice by deep learning. *Nat. Methods* **14**, 403–406 (2017).
90. Croce, A. C. & Bottiroli, G. Autofluorescence spectroscopy and imaging: A tool for biomedical research and diagnosis. *Eur. J. Histochem.* **58**, 320–337 (2014).
91. Nwankire, C. E. *et al.* Label-free impedance detection of cancer cells from whole blood on an integrated centrifugal microfluidic platform. *Biosens. Bioelectron.* **68**, 382–389 (2015).
92. van Waateringe, R. P. *et al.* Skin autofluorescence, a non-invasive biomarker for advanced glycation end products, is associated with the metabolic syndrome and its individual components. *Diabetol. Metab. Syndr.* **9**, 42 (2017).
93. Yung, M., Klufas, M. A. & Sarraf, D. Clinical applications of fundus autofluorescence in retinal disease. *Int. J. Retin. Vitr.* **2**, 12 (2016).
94. Ikeda, N. *et al.* Early detection of bronchial lesions using newly developed videoendoscopy-based autofluorescence bronchoscopy. *Lung Cancer* **52**, 21–27 (2006).
95. Lagarto, J. L. *et al.* Characterization of NAD(P)H and FAD autofluorescence signatures in a Langendorff isolated-perfused rat heart model. *Biomed. Opt. Express* **9**, 4961

(2018).
96. Rice, W. L., Kaplan, D. L. & Georgakoudi, I. Two-photon microscopy for non-invasive, quantitative monitoring of stem cell differentiation. *PLoS One* **5**, (2010).
97. Quinn, K. P. *et al.* Quantitative metabolic imaging using endogenous fluorescence to detect stem cell differentiation. *Sci. Rep.* **3**, (2013).
98. Arribas, S. M., Daly, C. J., González, M. C. & Mcgrath, J. C. Imaging the vascular wall using confocal microscopy. *Journal of Physiology* vol. 584 5–9 (2007).
99. Xu, J. & Shi, G.-P. Vascular wall extracellular matrix proteins and vascular diseases. *Biochim. Biophys. Acta - Mol. Basis Dis.* **1842**, 2106–2119 (2014).
100. Greenwald, S. Ageing of the conduit arteries. *J. Pathol.* **211**, 157–172 (2007).
101. Jaffe, M. *et al.* Transforming Growth Factor-β Signaling in Myogenic Cells Regulates Vascular Morphogenesis, Differentiation, and Matrix Synthesis. *Arterioscler. Thromb. Vasc. Biol.* **32**, e1-11 (2012).
102. Keeley, F. W. & Johnson, D. J. The effect of developing hypertension on the synthesis and accumulation of elastin in the aorta of the rat. *Biochem. Cell Biol.* **64**, 38–43 (1986).
103. Wanjare, M., Agarwal, N. & Gerecht, S. Biomechanical strain induces elastin and collagen production in human pluripotent stem cell-derived vascular smooth muscle cells. *Am. J. Physiol. Cell Physiol.* **309**, C271-81 (2015).
104. Nili, N., Zhang, M., Strauss, B. H. & Bendeck, M. P. Biochemical analysis of collagen and elastin synthesis in the balloon injured rat carotid artery. *Cardiovasc. Pathol.* **11**, 272–276 (2002).
105. Kothapalli, C. R., Taylor, P. M., Smolenski, R. T., Yacoub, M. H. & Ramamurthi, A. Transforming Growth Factor Beta 1 and Hyaluronan Oligomers Synergistically Enhance Elastin Matrix Regeneration by Vascular Smooth Muscle Cells. *Tissue Eng. Part A* **15**, 501–511 (2009).
106. Zimmerman, K. A. *et al.* Calreticulin Regulates Neointima Formation and Collagen Deposition following Carotid Artery Ligation. *J. Vasc. Res.* **52**, 306–20 (2015).
107. Krishnan, P. *et al.* Enhanced neointimal fibroblast, myofibroblast content and altered extracellular matrix composition: Implications in the progression of human peripheral artery restenosis. *Atherosclerosis* **251**, 226–233 (2016).
108. McCaffrey, T. A. TGF-βs and TGF-β receptors in atherosclerosis. *Cytokine and Growth Factor Reviews* vol. 11 103–114 (2000).
109. Pahk, K. *et al.* Visualization of Synthetic Vascular Smooth Muscle Cells in Atherosclerotic Carotid Rat Arteries by F-18 FDG PET. *Sci. Rep.* **7**, 6989 (2017).
110. Semenza, G. L. Hypoxia-inducible factors in physiology and medicine. *Cell* vol. 148 399–408 (2012).
111. Singh, S. J., Turner, W., Glaser, D. E., McCloskey, K. E. & Filipp, F. V. Metabolic shift in density-dependent stem cell differentiation. *Cell Commun. Signal.* **15**, 44 (2017).
112. Teslaa, T. & Teitell, M. A. Pluripotent stem cell energy metabolism: an update. *EMBO J.* **34**, 138–153 (2015).
113. Shyh-Chang, N. & Ng, H. H. The metabolic programming of stem cells. *Genes and Development* vol. 31 336–346 (2017).
114. Majesky, M. W. A Tangled Web of Metabolism and Transcription Controls SMC Phenotype. *Circulation Research* 57–59 (2020) doi:10.1161/CIRCRESAHA.119.316281.
115. Paredes, F., Williams, H. C., Quintana, R. A. & San Martin, A. Mitochondrial Protein Poldip2 (Polymerase Delta Interacting Protein 2) Controls Vascular Smooth Muscle

Differentiated Phenotype by O-Linked GlcNAc (N-Acetylglucosamine) Transferase-Dependent Inhibition of a Ubiquitin Proteasome System. *Circ. Res.* 41–56 (2020) doi:10.1161/CIRCRESAHA.119.315932.

116. Datla, S. R. *et al.* Poldip2 knockdown inhibits vascular smooth muscle proliferation and neointima formation by regulating the expression of PCNA and p21. *Lab. Invest.* **99**, 387–398 (2019).
117. Gomez, D., Shankman, L. S., Nguyen, A. T. & Owens, G. K. Detection of histone modifications at specific gene loci in single cells in histological sections. *Nat. Methods* **10**, 171–177 (2013).
118. Gunaratne, R. *et al.* Machine learning classification of human joint tissue from diffuse reflectance spectroscopy data. *Biomed. Opt. Express* **10**, 3889–3898 (2019).
119. Morrow, D., Cullen, J. P., Liu, W., Cahill, P. A. & Redmond, E. M. Alcohol inhibits smooth muscle cell proliferation via regulation of the Notch signaling pathway. *Arterioscler. Thromb. Vasc. Biol.* **30**, 2597–603 (2010).